ABSTRACT

Title of Document: A STUDY OF OPTICAL, PHYSICAL AND CHEMICAL PROPERTIES OF AEROSOLS USING IN SITU MEASUREMENTS

Zahra Chaudhry, Ph.D., 2009

Directed By: Professor Zhanqing Li, Department of Atmospheric and Oceanic Science

Using a simple sampling apparatus, aerosol particles were collected on a polycarbonate substrate in various locations around the world. The focus of this study was Xianghe, China, an industrial town 70 km southeast of Beijing. The Nuclepore filters were collected in two size ranges (coarse, $2.5\mu m < d < 10\mu m$, and fine, $d < 2.5\mu m$) from January-December 2005, with a focus on the Intensive Observation Campaign (IOC) in March 2005.

The collected filters were analyzed for aerosol mass concentration and aerosol absorption efficiency; selected filters were analyzed for chemical composition. For fine mode aerosols measured during the Xianghe 2005 IOC, the average spectral absorption efficiency equates well to a λ^{-1} model, while the coarse mode shows a much flatter spectral dependence, consistent with large particle models. The coarse mode absorption efficiency was compatible with that of the fine mode in the near-IR

region, indicating the much stronger absorption of the coarse mode due to its composition and sizeable mass.

Ground-based measurements were compared to remote sensing instruments that measure similar parameters for the total column. A co-located lidar assisted in determination of vertical homogeneity. For cases of vertical homogeneity, the ground-based measurements were able to represent total column measurements well. For cases of vertical inhomogeneity, ground-based measurements did not equate well to total column measurements.

The layers of aerosols that form in the atmosphere have significant effects on the temperature profile. An instrument was developed to measure aerosol absorption and scattering, the Scattering and Absorption Sonde (SAS). This instrument was launched seven times at two locations in China in 2008. Vertical profiles of scattering coefficient were measured and several aerosol layers were identified.

The aerosol characterized at Xianghe, China was compared to aerosol characteristics from Kanpur, India and Mexico City, Mexico. The aerosol at Mexico City differs greatly from that at Xianghe, based on the measured mass concentration, aerosol size distribution from AERONET, and measured aerosol absorption efficiency. The aerosol at Kanpur resembles well the aerosol characterized at Xianghe in the fine mode, with a correlation of 0.998 for the aerosol absorption efficiency.

A STUDY OF OPTICAL, PHYSICAL AND CHEMICAL PROPERTIES OF AEROSOLS USING IN-SITU MEASUREMENTS

By

Zahra Chaudhry

Dissertation submitted to the Faculty of the Graduate School of the
University of Maryland, College Park, in partial fulfillment
of the requirements for the degree of
Doctor of Philosophy
2009

Advisory Committee:
Professor Zhanqing Li, Chair
Professor Russell R. Dickerson
Dr. A. Jay Kaufman
Dr. J. Vanderlei Martins
Dr. Jeffrey W. Stehr

Preface

This document contains original scientific content produced by the author and collaborators. Significant scientific findings include:

- In situ measurements of aerosol absorption efficiency for one year from Xianghe show a shift in the fine mode absorption efficiency from one season to the next with the lowest absorption in the summer, the greatest in the winter, and fall and spring falling in between. The coarse mode absorption efficiency separates into two groups: fall, winter and spring have similar absorption, while summer has much lower absorption through the whole measured spectrum.

- Intercomparison between a laboratory-based technique (optical reflectance, OR) and a commercially-available instrument (PSAP) demonstrates the strength of the OR technique.

- Demonstrating that ground-based in situ measurements compare well with ground-based remote sensing instruments when the aerosol is distributed evenly through the total column.

- Detailing the chemical composition of the aerosols collected during the IOC at Xianghe, and demonstrating a source apportionment via Absolute Principle Component Analysis. Each sampled mode was determined to derive from four sources, with the fine mode resolving 68% of the variability in these sources, and the coarse mode resolving 88% of the variability. The remaining variability is undefined.

- Detailing the concept behind a balloon-borne scattering-and-absorption sonde. Ground validation with a HEPA filter and intercomparison with a co-located nephelometer increases our confidence in the accuracy of the measured scattering coefficient.

- Comparing the aerosol mass concentration and absorption efficiency measured during the IOC at Xianghe with samples collected at other urban, dust-influenced locations. We present cases where the aerosols correlate well (such as the fine mode aerosols at Xianghe and Kanpur, India) and when the correlation is poor (coarse mode aerosols at both Mexico City and Kanpur correlate poorly with Xianghe).

Published papers based on this work:

Chaudhry, Z., J.V. Martins, Z. Li, S.-C. Tsay, H. Chen, P. Wang, T. Wen, C. Li and R.R. Dickerson (2007), In situ measurements of aerosol mass concentration and radiative properties in Xianghe, southeast of Beijing, *J. Geophys. Res., 112*, D23S90, doi:10.1029/2007JD009055.

Dedication

To my parents, who taught me to never stop learning.

To my soon-to-be husband, who has cheered me on every step of the way.

Acknowledgements

The work presented in this study would not be possible without the tremendous support of my two advisors. Dr. Zhanqing Li encouraged my work in China, and his amazing ability to review any material I sent him (proposals, papers, posters, etc), usually within a day, gave me the feedback and confidence I needed to continue my efforts. Dr. J. Vanderlei Martins taught me so much about in situ measurements, data analysis and instrumentation. From turning his kid's toys into instruments, to solving problems in the field using everyday items, I would not have been able to turn out such a robust data set without his expertise.

I would like to thank the numerous collaborators whose hard work in the field contributed to a robust data set of in situ measurements. In Mexico: Dr. Andrea Castanho, Mr. Dominik Cieslak and Dr. Roberto Fernandez-Borda. In India: Dr. Lorraine Remer, Mr. Rich Kleidman, and Mr. Ravi Mishra. In China for the 2005 IOC: Dr. Tianxue Wen. In China for the 2008 campaign: Dr. Tianxue Wen, Dr. Qiang Ji, Dr. Si-Chee Tsay, Mr. Shaun Bell, and Dr. Wu Zhang.

Samples were maintained meticulously in the laboratory at the NASA Goddard Space Flight Center, and I would like to thank Yacov Kleidman and Matis Kleidman for their many back-breaking hours spent weighing filters and carrying out reflectance measurements. I would like to thank Debbie Thomas from NASA-GSFC for the use of her microbalance scale, and for the use of her time and expertise on the Scanning Electron Microscope.

Data were used in this study that were collected from other research groups. Namely, I would like to thank the University of Maryland Atmospheric Chemistry group for the use of their PSAP and TSI Nephelometer data, the NASA SMART-COMMIT group for their TSI Nephelometer data, the AERONET group for the easy access to data, and the MPLnet group for the Xianghe lidar scans.

I would like to thank Gergely Dolgos from UMBC for running the PIXE samples in Brazil, and for providing the calibrated, calculated concentrations. I would also like to thank Alex Correia and Manfredo Tabachnik for their time, assistance, and patience with the APCA analysis.

Lastly, I would like to thank Dominik Cieslak from UMBC for his engineering expertise, time and patience as we developed the SAS, and to Li Zhu at UMBC for all her time spent testing the SAS.

Table of Contents

List of Tables

List of Figures

Chapter 1: Introduction

1.1 Motivation

According to the Fourth Assessment Report (FAR) of the Intergovernmental Panel on Climate Change (IPCC), the radiative forcing of aerosols is still an area of great uncertainty [*IPCC*, 2007]. The uncertainty in the total direct aerosol radiative forcing has been reduced, but there is more uncertainty in the radiative forcing of individual aerosol species, where in many cases, the uncertainty is just as large as the forcing itself. Nitrate is one such example; the radiative forcing is estimated to be -0.1 ± 0.1 Wm^{-2}. Organic carbon from fossil fuel combustion is another; the radiative forcing is estimated to be -0.05 ± 0.05 Wm^{-2}. The total radiative forcing by aerosols is estimated to be negative, offsetting the positive forcing by greenhouse gases of $+2.63 \pm 0.26$ Wm^{-2} [*IPCC*, 2007].

The influence of aerosols on climate is more complex than that of the greenhouse gases [e.g., *Schwartz and Buseck*, 2000]. Aerosol distribution is variable both spatially and temporally, and although aerosol lifetimes are shorter than those of greenhouse gases, estimates of their atmospheric residence times range from less than a day to more than a month, resulting in transport distances from a few kilometers to hemispheric scales [*Marley et al.*, 2000, *Williams et al.*, 2002]. Aerosols can be transported to regions far from their origin by lifting mechanisms that carry them across continents and oceans. These aerosol layers can influence local and regional climate and also mix with local aerosols. In cases where the vertical distribution of aerosols is fairly uniform, ground-based measurements are able to represent the optical properties of aerosols in the total column. This is highly desirable, as ground-

based measurements are relatively easy to acquire, cost-effective, and can offer good spatial and temporal resolution.

The complexity of quantifying the effect that aerosols have on local and regional climate increases substantially when one considers how optical properties change as aerosols mix in the atmosphere [*Jacobson*, 2000]. Aerosol composition can be highly variable, with different species present within the same particle, due to different sources, production mechanisms and atmospheric reactions [*Posfai et al.*, 1999]. In addition, these different species can be either internally or externally mixed within the particle yielding different optical and microphysical properties and different radiative effects [*Posfai et al.*, 1999, *Martins et al*., 1998, *Schnaiter et al*., 2005]. This variability in composition and distribution makes it difficult to quantify the aerosol impacts on climate and to represent these effects in climate models.

According to the IPCC's Fourth Assessment Report, our ability to quantify the direct effect of aerosols on the global climate is hindered by uncertainties in the measurements of aerosol absorption [*Forster et al.*, 2007]. The sign and magnitude of the direct aerosol forcing at the top of the atmosphere are dictated by single scattering albedo (ω_0), aerosol optical thickness (τ), surface albedo, and scattering phase function [*Coakley and Chylek*, 1975].

Remote sensing techniques such as satellites and ground-based sun photometers, including the Aerosol Robotic Network, AERONET [*Holben et al*., 1998], are better at measuring the total column amount of aerosols than most ground-based in situ instruments. Passive satellite remote sensing also offers excellent spatial coverage but, depending on the vertical structure of the atmosphere and surface

reflectance, it can have problems measuring the aerosol concentration near the ground. The narrow swath of space-borne lidars (e.g., CALIPSO, *Winker et al.* [2003], GLAS, *Zwally et al.* [2002]) may provide good assessment of the vertical distribution of aerosols and clouds, but do not provide global coverage like the passive instruments. The drawback of column mean values is that they can have little meaning for near-surface effects if large concentrations of aerosols are in higher layers. Besides, collecting aerosol samples on the ground level also provides the advantage of studying their impact on health, as they are a known health risk.

1.2 Aerosol Physical Properties

The mass concentration of aerosols, reported in mass of aerosol per unit volume of air, is a measure of the loading of aerosols in the atmosphere. There are currently three ways of measuring aerosol mass concentration: the gravimetric method, the analytical method, and via optical methods [*Agranovski*, 2000]. The most common method to measure aerosol mass concentration is the gravimetric method, which was used in this study. A known volume of air is passed through a filter and the increase in mass of the filter due to the collected aerosol particles is measured. To make these measurements, one must be able to weigh accurately a filter before and after sampling and accurately measure the sampling flow rate and sampling time. A commercially-available instrument that uses this method is the TEOM (Tapered Element Oscillating Microbalance) from Thermo Scientific.

The analytical method involves collection of aerosol samples for subsequent quantitative chemical or physical analysis. Once aerosol particles are separated from the ambient air, usually by drawing air through a filter, the particles can be analyzed

via chemical and spectrographic analysis, optical analysis, or x-ray diffraction. Instruments such as the Aethelometer [*Hansen et al.,* 1982] use the optical method where the beam of light passes through the particles within a filter medium. The intensity of the optical beam is attenuated proportionally to the number of particles in the filter. A number of assumptions of aerosol optical properties and light attenuation within the filter medium go into this particular method.

Aerosols can also be described physically by their size distributions. As a result of the effect of air pollution on health, particles less than 2.5 μm in diameter are generally referred to as "fine", and those greater than 2.5 μm in diameter are "coarse". These two modes, in general, originate separately, undergo different transformation processes, are removed from the atmosphere by different mechanisms, have different chemical composition, different optical properties, and differ significantly in their deposition patterns in the human respiratory tract. Any discussion of physics, chemistry, measurement, or health effects of aerosols must distinguish between these two size categories [*Seinfeld and Pandis*, 1998]. TSI's Aerodynamic Particle Sizer (APS) measures, in situ, the size distribution of particles from 0.5 to 20 μm aerodynamic diameter [*Volkens and Peters*, 2005]. The instrument both counts and measures the size of the particles using the light scattering of the particles and settling velocity. Size distributions can also be measured by remote sensing. AERONET measures the size distribution of particles by inverting the sun photometer radiance measurements from almucantar and principle plane scans.

Aerosols can also be physically characterized by their number concentration, which is the number of aerosol particles in a given volume of air. TSI's

Condensation Particle Counters (CPC) typically count particles with a diameter between 5 nm to >3000 nm. As it is very hard to detect sub-micron-sized particles optically (since the diameter is very close to, or smaller than, the wavelength of light), the diameter of the particles is increased before detection. The particles are passed through a chamber saturated with evaporated alcohol, which condenses on the surface of the particle, making it larger and easier to detect/count.

1.3 Aerosol Optical Properties

The global radiation budget is significantly influenced by how aerosols interact with radiation. This interaction between aerosols and radiation is a fundamental property that needs to be accounted for in aerosol models. There are numerous ways in which aerosol optical properties can be described, including optical depth, scattering and absorption coefficients, single scattering albedo, refractive indices, scattering phase function, and asymmetry parameter.

Aerosol optical depth (τ) is defined as the attenuation of a light beam during its path through a medium. If I_0 is the intensity of radiation at the source, and I is the observed intensity after a given path, then optical depth (τ) is defined by:

$$\frac{I}{I_0} = e^{-\tau}$$

Aerosols can attenuate the light beam by either scattering, or absorption of the photons. When aerosols in the atmosphere scatter radiation upwards, they can prevent that radiation from reaching the Earth's surface, thereby cooling the surface. When atmospheric aerosols absorb radiation, they warm the surrounding air, and also prevent the radiation from reaching the Earth's surface. By heating a layer of air

above the surface, the aerosols stabilize the atmosphere, which has numerous consequences, including decreased cloud formation [*Koren et al.*, 2008], reduced surface evaporation, and trapping pollutants near the ground by forming an inversion. Various instruments such as the Integrating Plate [*Lin et al.*, 1973], Particle/Soot Absorption Photometer (PSAP, Radiance Research, Seattle, WA), Aethalometer [*Hansen et al.*, 1982] and other filter-based measurements have been used to obtain data on aerosol absorption, while newer instruments such as the photoacoustic spectrometer [*Arnott et al.*, 1999] and the cavity ringdown spectrometer [*Sappey et al.*, 1998] measure absorption without the use of a filter substrate. Aerosol scattering is usually measured by nephelometry, which employs a light beam and a light detector set to avoid the direct incident of the light beam. The light reflected from particles intercepting the beam is measured. There are a few manufacturers who produce research-grade nephelometers for in situ measurements of aerosol scattering, such as TSI (St. Paul, MN) and Radiance Research (Seattle, WA).

Aerosol Optical Depth-AOD (or Aerosol Optical Thickness-AOT as it is sometimes called) is measured most commonly by remote sensing. Ground-based instruments such as Microtops sunphotometers and AERONET's Cimel sunphotometer both retrieve AOD from direct solar radiation measurements [*Holben et al.*, 1998]. The measurement site location and elevation are needed to process the measurement into an AOD product.

Single-scattering albedo (ω_0 or SSA), is often used to describe aerosol optical properties and is defined as the ratio between scattering and extinction coefficients,

where the extinction coefficient is the sum of the scattering and absorption coefficients:

$$\omega_0 = \frac{\beta_{scat}}{(\beta_{scat} + \beta_{abs})}$$

SSA is the relative probability that a photon that interacts with the aerosol particles will be scattered or absorbed. If $\omega_0 = 1$, then the photon is scattered, whereas if $\omega_0 = 0.10$, then the probability that the photon is scattered is 10%. SSA can be calculated from any measurements of absorption and scattering coefficients that are made at the same wavelength and in the same units. It can also be derived using data from remote sensing platforms, such as AERONET, which produces ω_0 as an inversion product.

The refractive index of a substance is best described as a complex number. The real part of the number is the "ordinary" refractive index, while the imaginary part indicates the amount of absorption. Both parts depend on wavelength. The imaginary part can range from 0 (non-absorbing) to 1 (absorbing), and is usually derived from size distribution and extinction measurements [*Spindler et al.*, 2007].

The phase function of aerosols describes the anisotropy of the scattering. It provides a factor of each direction with which the incoming intensity has to be multiplied to give the outgoing intensity. *West et al.* [1997] measured the phase function of dust in a laboratory chamber at three wavelengths in the visible and near-IR. The particles scattered light as they fell through the chamber, and half of the samples measured agreed well with the theoretical phase function for spherical particles, while the other half of the samples did not. The authors postulate that those

samples could differ from theory due to very high refractive indices or different particle microstructures.

Related to the phase function, the aerosol asymmetry parameter (g) is defined as the cosine-weighted average of the phase function. It is commonly used in large scale radiative transfer models to describe the angular distribution of light scattering as it is more efficient (computationally) than computing the scattering phase function in already complex codes. While g cannot be measured directly, it can be calculated. In situ measurements of total backscatter (β_{scat}) and hemispheric backscatter (β_{bscat}) can be used to calculate g using the Henyey-Greenstein model [*Andrews et al.*, 2006]. In situ measurements of aerosol size distribution can also be used to derive g using Mie calculations [*Andrews et al.*, 2006]. Remote sensing techniques such as the AERONET sunphotometers and the AATS-14 sun photometer calculate g from inversion algorithms.

1.4 Aerosol Chemical Properties

The chemical composition of aerosols is important to determine aerosol sources, and plays an important role in transforming aerosols over time. Aerosols can be generalized into two major types: anthropogenic (man made biomass burning, vehicular exhaust, industrial processes, etc.) and natural (biogenic emissions from forests, sea salt, volcanic eruptions, most dust episodes, etc.). The description of the aerosol type also gives an idea of the chemical composition.

Many different instruments and measurement techniques are used to quantify the chemical composition of aerosols. The amount of organic (OC) and elemental carbon (EC) can be determined by an OC/EC analyzer, where aerosol samples

collected on preconditioned quartz filters are heated in four stages and the vaporized sample is measured as CO_2 or CH_4. The ratio between OC and EC gives a sense of the aerosol source. For example, biomass burning has greater OC than EC, while diesel engine exhaust has higher EC than OC. Concentrations of non-carbon elements can be obtained from various mass spectrometry techniques (i.e. inductively coupled plasma mass spectrometry-ICP-MS), Particle-Induced X-ray Emission (PIXE), X-ray Florescence, and ion/gas chromatography. As PIXE is used in this study, it will be outlined in Section 3.1.

Another aerosol property that falls under the category of chemical properties is aerosol hygroscopicity (f), as it depends directly on the aerosol composition. Aerosols can be hygroscopic, attracting water, or hydrophobic, repelling water. As hygroscopic aerosols attract water and grow, their optical properties change. The rate at which the particles hydrate, or dehydrate, varies according to their composition. This growth factor, known as the aerosol hygroscopic growth factor (f) is important for radiative transfer models to accurately account for particle size distribution changes as a function of relative humidity. It can be calculated from in situ techniques by making a series of measurements of light scattering at a variety of humidity levels. The ratio between the enhanced RH β_{scat} and the reference β_{scat} is the hygroscopic growth factor. It can also be calculated from remote sensing techniques. *Pahlow et al.* [2006] did so with a Raman lidar, assuming a boundary layer well-mixed in aerosol, potential temperature and water vapor. The authors compared this method with ground-based in situ measurements of f, and found good agreement in some cases, poorer agreement in other cases.

1.5 EAST-AIRE overview

The rapid population and economic growth seen in China over the last few decades has had strong effects on the local and regional air quality and climate. The increase in manufacturing and demand for products has led to serious air quality concerns. Several intensive studies have been conducted recently to examine the transport of air masses from the region over the Pacific, such as the Asian-Pacific Regional Aerosol Characterization Experiment (ACE-Asia) [*Huebert et al*., 2003], the Asian Atmospheric Particle Environment (APEX) [*Nakajima et al.*, 2003] and the NASA Global Tropospheric Experiment Transport and Chemical Evolution Over the Pacific (TRACE-P) [*TRACE-P Science Team*, 2003]. The East Asian Study of Tropospheric Aerosols: an International Regional Experiment (EAST-AIRE) takes a closer look at the physical, optical and chemical properties of aerosols across China through a series of ground-based observation stations [*Z. Li et al*., 2007]. EAST-AIRE was established as a joint research venture between the U.S. and China with the goal of acquiring and understanding the physical, chemical, and optical properties of the dominant natural and anthropogenic aerosols and their precursor gases in China, and to gain insights into the direct and indirect effects of these aerosols on radiation, clouds, precipitation, atmospheric circulation and the environment [*Z. Li et al.*, 2007].

EAST-AIRE is unique in the combination of ground-based, aircraft, and remote sensing platforms, all connected to achieve the program goals outlined above. The program includes two baseline observatories (Xianghe and Taihu) where extensive measurements were made starting in 2005, including: radiative quantities using broadband and narrowband radiometers and spectrometers, cloud properties,

aerosol optical properties retrieved from Cimel Sun Photometers and Multi-Filter Rotating Shadowband Radiometers (MFRSR), and physical and chemical properties from several aerosol impactor samples. In addition to the baseline sites, there was an aircraft and intensive ground campaign in Liaoning in April 2005, and in March, 2005, the Xianghe baseline site hosted an Intensive Observation Campaign (IOC). Many instruments measuring similar parameters were run side-by-side to calibrate newer instruments against well-used and well-characterized instruments, as well as to ensure accurate measurements across various levels of resolution.

1.6 Scientific objectives of this work

1. To gain further knowledge on the local and transported aerosol at Xianghe, China by utilizing a year-long record of filter-based optical, physical and chemical measurements and other co-located instrumentation.
2. To examine the vertical profile of extinction by launching a "scattering-and-absorption sonde" (SAS).
3. To compare the measured aerosol absorption efficiency and aerosol mass concentration at a range of urban-influenced locations.

<u>Questions to be addressed</u>

Objective 1:

- How well does the Optical Reflectance technique compare to readily-available commercial equipment, such as the PSAP?
- How well do ground-based measurements represent the total aerosol column?

- Is there seasonal variability in the absorption efficiency? What does this tell us about the composition of the seasonal aerosol? Is the variability due to polluting patterns, or circulation changes?
- Can the chemical composition of the ground-based aerosol samples give us information on aerosol sources?

Objective 2:

- How well does the SAS measure β_{scat} and β_{abs}?
- Can the SAS resolve layers of aerosols? How do the layer optical properties differ from those of the ground-level aerosol?

Objective 3:

- Will the differences in the many datasets used here significantly hamper our ability to compare these measurements? Some of the variables are relative humidity, sampling season, sampling duration, sampling altitude, etc.
- The sites chosen for this comparison have significant urban aerosol loading from anthropogenic sources as well as a transported dust source. Does this similarity in aerosol sources translate to similarities in the aerosol optical and physical properties?

Chapter 2: Aerosol Optical and Physical Properties in Xianghe, China during 2005

2.1 Methodology

A two-stage sampling apparatus was installed at Xianghe, China in January, 2005 to collect aerosol particles on Nuclepore filters (Figure 2.1). These polycarbonate filters have a smooth surface with randomly distributed pores that ensure a designated particle size cutoff. The system has an impactor inlet ensuring a 10 μm aerodynamic diameter cut-off size, and the impactor is coated with Apiezon grease to reduce particle bounce [*Hopke et al.,* 1997]. The first filter collects particles larger than 2.5 μm (hereafter referred to as the coarse mode) and the second filter collects particles less than 2.5μm aerodynamic diameter (hereafter referred to as the fine mode) [*John et al.,* 1983]. The filters are placed in a Stacked Filter Unit (SFU) which optimizes the distance between the filters and ensures the size cut-off [*Parker et al.,* 1977].

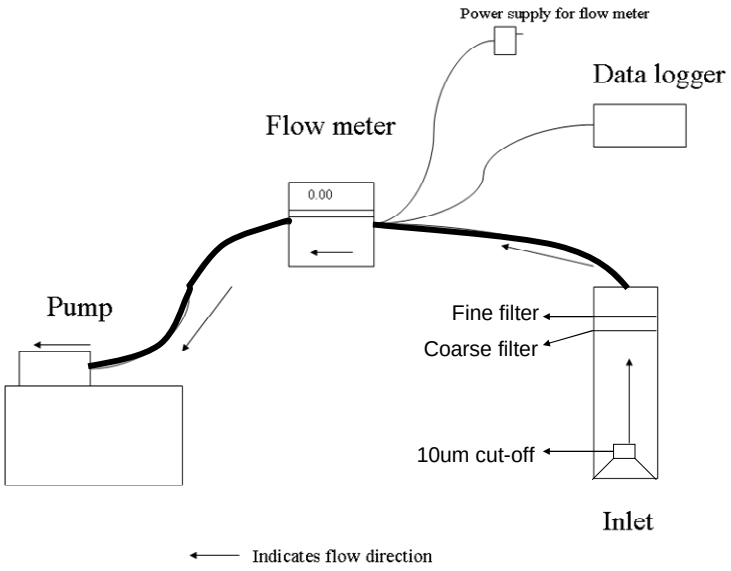

Figure 2.1 Basic sampling apparatus for collecting Nuclepore filters in Stacked Filter Units (SFUs) which separate particles into a coarse mode and fine mode.
Arrows indicate air flow through system such that the diaphragm pump is drawing the air through the flowmeter, filters and inlet. Dark lines indicate air flow tubing, while lighter lines denote electrical connections.

Size-resolved filters were collected twice daily up to and through the IOC (January-March) and collected once daily for the rest of the calendar year, with a few gaps due to instrument or supply-related problems. The filters were changed between 6-7 a.m. and between 7-8 p.m., local time, to roughly coincide with sunrise and sunset. The initial flow through the filters was set at 18 lpm (liters per minute) manually and only filters with a final flow of greater than 8 lpm were analyzed. The instantaneous flow rate was recorded in a data logger and utilized in data analysis to correct for flow changes during sampling.

The filters were subjected to gravimetric analysis prior to and after field deployment. Blank filters were sent to the field amongst the exposed filters and were treated similarly to monitor the whole process. The filters were exposed to an ionizer for 24 hours prior to weighing to remove static charge and to ensure an accurate mass

measurement. The humidity in the ionizing chamber was recorded for each cycle and maintained around 20%. The humidity of the weighing room was also recorded at around 40%. The difference in humidity was determined not to affect the particles on the filters. Since the particles were collected at a variety of humidity levels, but analyzed dry, the higher humidity of the weighing room was not great enough to rehumidify the particles. According to meteorological data at the measurement site in Xianghe, the local humidity level stayed relatively low, averaging 36% during the IOC [*C. Li et al*., 2007].

After gravimetric analysis, the filters are subjected to an optical reflectance (OR) technique previously applied in *Martins et al.* [1998], and validated against an extinction cell and PSAP measurements in *Reid et al.* [1998]. The filter is placed on a diffusive Spectralon panel and illuminated from above. The amount of light reflected (ρ) is measured from 350 nm to 2500 nm by an ASD LabSpec Pro spectrometer (Analytical Spectral Devices, Boulder, Colorado), with radiometric stability of 1% and accuracy of approximately 3% [*Kindel et al*., 2001]. By passing light through the particles and reflecting the light off the filter and the Lambertian surface below, we are essentially mimicking the same method used by satellite sensors. This technique has the advantage that we can characterize well the bright surface underneath the particles. Blank filters are also placed on top of the Spectralon panel and measured as a reference for the reflectance method (ρ_{surf}). For the 2-way transmission:

$$\rho = \rho_{surf} \cdot T_1 \cdot T_2 \qquad \text{Eq. 1}$$

And each transmission term is defined as:

$$T = \exp\left[-\frac{\tau_{abs}}{\cos\theta} \right]$$

Eq. 2

where θ is the zenith angle of illumination or detection.

Solving these two equations for the measured reflectance:

$$\rho = \rho_{surf} \bullet \exp\left[-\frac{2\tau_{abs}}{\cos\theta \bullet \cos\theta_0} \right] \qquad \text{Eq. 3}$$

Aerosol absorption optical depth (τ_{abs}) from Eq. 2 can be defined as

$$\tau_{abs} = \sigma \cdot \alpha_a \qquad \text{Eq. 4}$$

Where α_a = aerosol total mass column (g/m^2)

σ = aerosol absorption efficiency (m^2/g)

Using Eq. 4 to solve Eq. 3 for σ (from *Martins et al*. [submitted, 2009] (hereafter referred to as *Martins et al.* [2009])):

$$\sigma = -\frac{\cos\theta \bullet \cos\theta_o}{2 \cdot \alpha_a} \ln\left(\rho / \rho_{Surf}\right) \qquad \text{Eq. 5}$$

Since the aerosol particles are collected on the surface of Nuclepore filters, we expect fewer optical artifacts with this method than with particles collected inside the fibers of quartz, Teflon or paper filters [*Clarke*, 1982]. The main optical artifacts observed on particles collected on the surface of Nuclepore filters come from an increased proximity between particles as a function of filter loading. The interaction between close particles and the fact that they are touching the surface of the filter produce non-linearities in the Beer-Lambert Law that can be modeled by a power law function. A calibration curve of this power law using artificial absorbing particles with known optical properties and a variety of mass loading is presented in *Martins et al*. [2009].

The absorption coefficient was calculated from the filters by utilizing the OR absorption efficiency at 550 nm and was compared with PSAP results at 574 nm,

which was operated in parallel with the filter sampling apparatus. The 550 nm wavelength was chosen to compare with the 3-λ TSI Nephelometer used during the IOC. Data from the University of Maryland's PSAP were obtained during the IOC at 5-minute intervals, corrected according to *Bond et al.* [1999], and extrapolated to 550 nm following *Virkkula et al.* [2005]. The University of Maryland's instruments are detailed in *C. Li et al.* [2007]. Since the filters were collected over approximately 12-hour intervals, the PSAP data were averaged over the same time period as the corresponding filter. The PSAP averages were also weighted according to the flow through the Nuclepore filter to account for the decrease in flow throughout the sampling period. This procedure ensured that both instruments sampled the aerosols similarly. This same process of averaging for sampling time and weighting for flow was applied to data obtained from the University of Maryland's 3-λ TSI Nephelometer. The Single Scattering Albedo (ω_0) was calculated using the absorption coefficient from the PSAP and from the OR and the scattering coefficient from the Nephelometer at 550 nm. The PSAP and Nephelometer were deployed on the same observatory tower as the filter sampling apparatus, but they did not include an upper-limit cut-off size like the 10 μm inlet used for the filters [*C. Li et al*., 2007].

2.2 Seasonal Aerosol Absorption Efficiency during 2005

The absorption efficiency is an important variable connecting the aerosol absorption properties and the aerosol particle mass concentration, and can be used in chemical transport models to connect chemistry and optical properties. The absorption efficiency is measured from the exposed Nuclepore filter using an optical reflectance technique and the mass measurements [*Martins et al*., 2009]. The spectral

dependence data provides important information on the average size of the absorbers, and some hints on the imaginary refractive index [*Martins et al.*, 1998].

Following the methodology outlined in Section 2.1, the reflectance was measured from the sampled filters and the aerosol absorption efficiency was calculated. The fine mode absorption efficiency shows variability from one season to the next (Figure 2.2). The highest absorption efficiency is seen in the winter months (blue line), while the lowest is seen in the summer months (pink line), and the fall and spring months lie between these two extremes. In comparison to the model for small absorbing particles with the spectral dependence λ^{-1}, the spectra of the summer absorption efficiency is the closest fit. Comparing all the seasons to λ^{-1}, the deviation from this model becomes apparent (Figure 2.3). While all the seasons fit to a straight line from 550 nm to 1550 nm, the deviations at the shorter wavelengths indicate the strength of the dust or organic carbon presence on those sampled filters. The summer absorption efficiency is the bottom line, and follows λ^{-1} through the spectrum. The next curve, spring, deviates slightly, then fall deviates more. Finally, winter has the largest separation from the λ^{-1} model. This could mean that there is more dust/OC present in the fine mode in the cooler months, or that the winter-time dust/OC is more absorbing than that in the spring or fall.

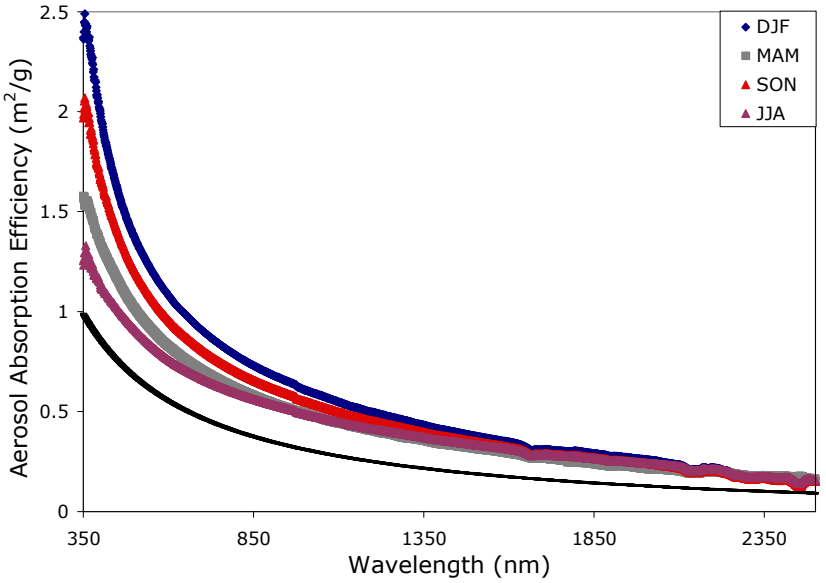

Figure 2.2: Fine mode spectral absorption efficiency by season at Xianghe during 2005. The black curve at the bottom represents the λ^{-1} model for small absorbers.

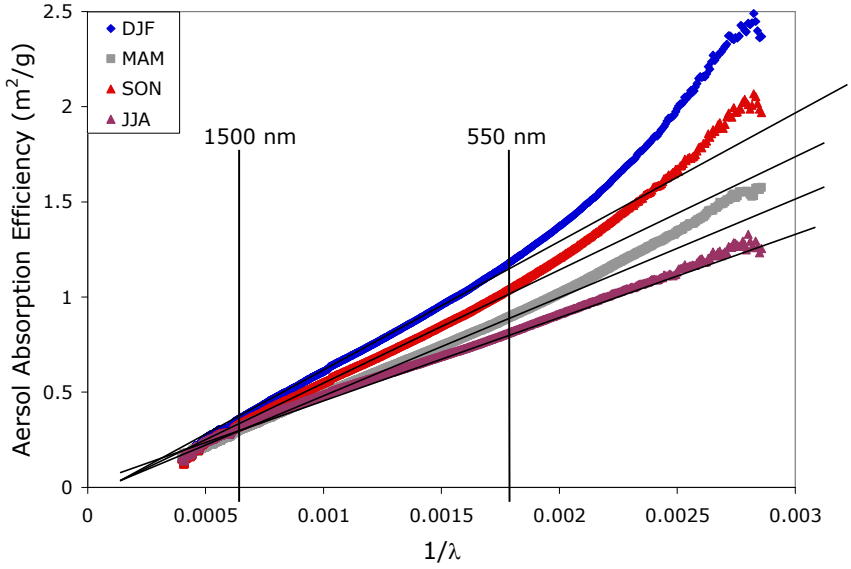

Figure 2.3: Fine mode seasonal spectral absorption efficiency versus the λ^{-1} model for small absorbers.
Deviations from a straight line at shorter wavelengths indicate the strength of the dust influence.

The coarse mode aerosol absorption efficiency is plotted by season in Figure 2.4. The winter (blue line) and fall (gray line) spectra are very similar, following one another through the whole measurement range. The spring absorption efficiency follows the winter and fall for longer wavelengths, but deviates to lower absorption

from 550 nm to 350 nm. This is indicative of a stronger dust influence on the absorption efficiency measurement in the fall and winter seasons. The summer coarse mode absorption efficiency is much less than the three other seasons throughout the whole measured spectra. Due to the prevalent monsoon rains in the summer, coarse mode particles are washed out efficiently. Also, the cooler months (fall, winter, and spring) would be more influenced by soot and dust, which is seen clearly in this data by the enhancement of absorption throughout the whole measured spectrum.

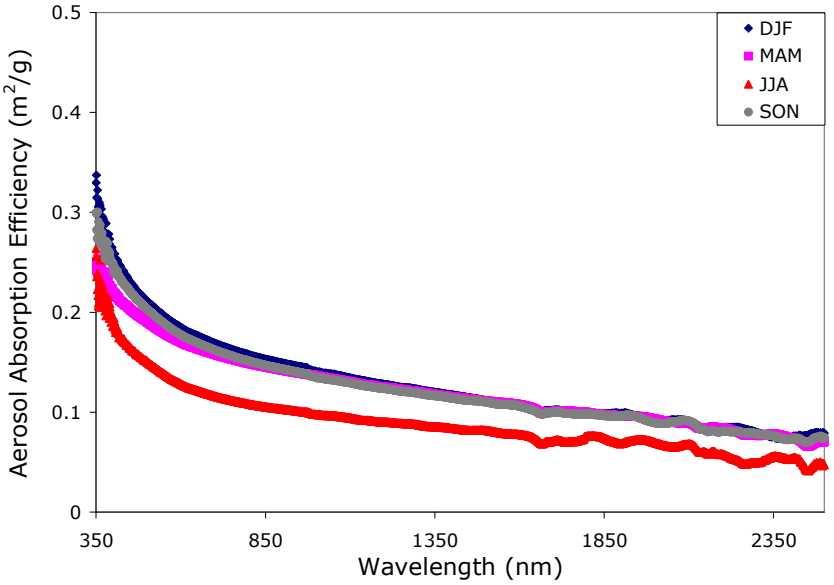

Figure 2.4: Coarse mode spectral aerosol absorption efficiency by season at Xianghe during 2005.
The lowest absorption efficiency is measured in the summer, when large particles are washed out by monsoon rains.

2.3 Optical Properties of Aerosols during the IOC

2.3.1 Aerosol Absorption Efficiency

In Figure 2.5a, the absorption efficiency of the coarse mode filters is shown as an average (black line) and one standard deviation (shaded) of the 35 filters that were

collected during the IOC. A second line is plotted (gray) showing a λ^{-1} spectral dependence consistent with small absorbers, usually smaller than 0.2 µm diameter and flat imaginary refractive index, like black carbon [*Martins et al*., 1998, *Bergstrom et al*., 2002]. The absorption efficiency of the coarse mode has a much flatter spectral dependence than the λ^{-1} line, which is consistent with larger particles with flat refractive indices possibly representing large black carbon cluster aggregates or combinations between dust particles and black carbon [*Martins et al*., 1998]. However, the fine mode filters absorption efficiency is very similar to the λ^{-1} model, as shown in Figure 2.5b. Departures from the λ^{-1} curve for small absorbing particles can be related to relatively fast changes in the imaginary component of the refractive index which is commonly observed in the short-wavelength visible and the UV for organic materials [*Chang and Charalampopoulos*, 1990, *Kirchstetter et al.*, 2004], nitrated or aromatic aerosols [*Jacobson*, 1999], or dust.

The fine and coarse mode absorption efficiencies are compared side-by-side in Figure 2.5c. While the fine mode is a more efficient absorber in the UV and visible regions, in the near-IR, both modes are equally good absorbers, indicated by the overlapping error bars. Much of the incoming solar radiation is absorbed in this region of the spectrum, and since the coarse mode mass is much greater than that of the fine (discussed in later sections), the large absorption by the coarse mode is significant and is rarely taken into account in climate studies.

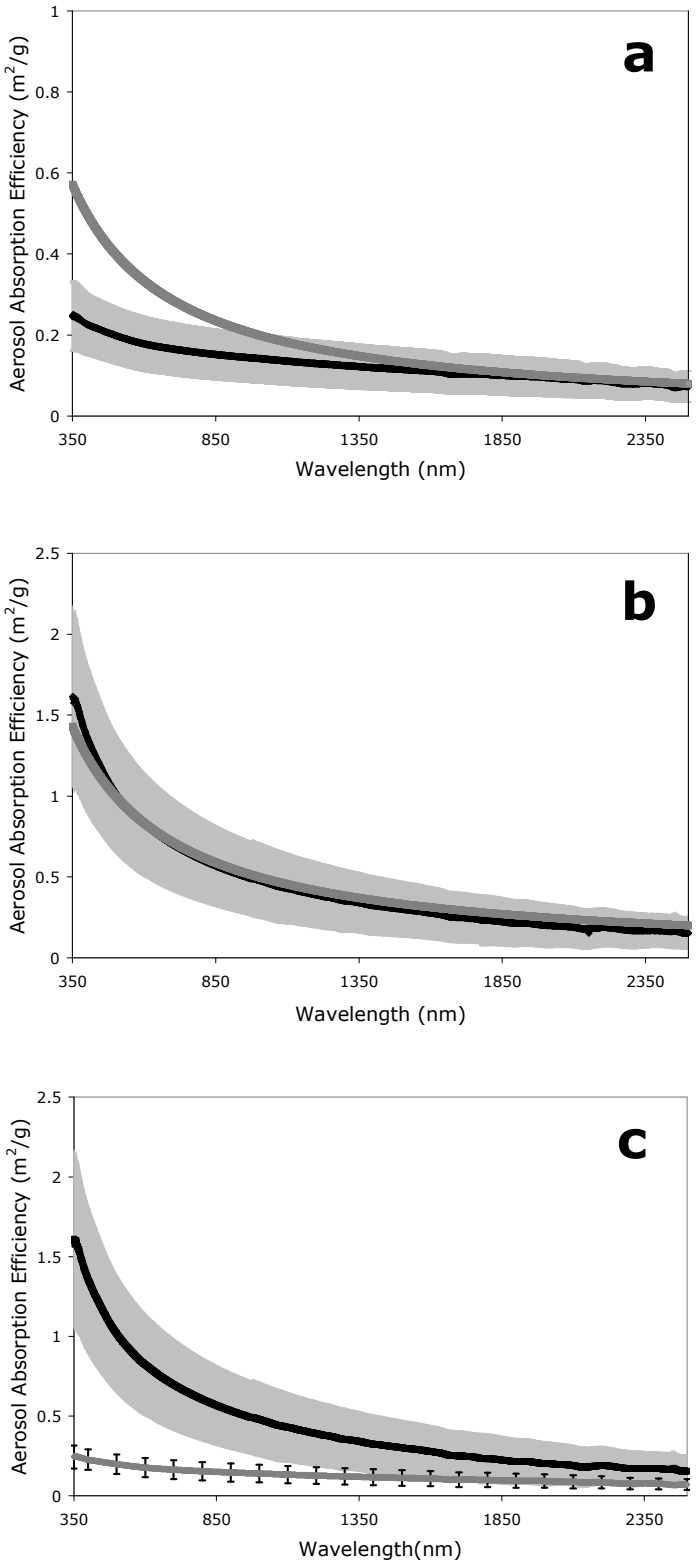

Figure 2.5: Spectral absorption efficiency (black line) for aerosol particles of a) 2.5 µm < d < 10 µm and b) d < 2.5 µm averaged from 35 filters from March 3-19, 2005 compared to a λ^{-1} model (gray line), then compared to each other in c.

The shaded area in each case represents the standard deviation of the measured cases. The error bars in figure c are equivalent to the shaded area in the figure a plot, but are shown as error bars for visual clarity.

The typical fine and coarse particles collected in Xianghe during the IOC were observed by the use of a scanning electron microscope (SEM) on sections of the filter. Pictures were taken of several representative filters with the scanning electron microscope at the NASA Goddard Space Flight Center in Greenbelt, MD. Figure 2.6a shows an example for the filter collected on March 10th, 2005, where the fine-mode filter shows a combination of spherical particles and aggregates of much smaller particles. The black circles represent the filter pores while the particles are pictured in shades of white and gray. The 1 µm scale on the bottom left corner indicates that all particles are smaller than 2.5 µm. The coarse mode filter SEM in Figure 2.6b shows large particles, probably composed of a combination of dust, black carbon, and organic material, from March 12th, 2005. The mixture between dust and black carbon could justify some of the absorption efficiency spectral dependence observed in Figure 2.5a.

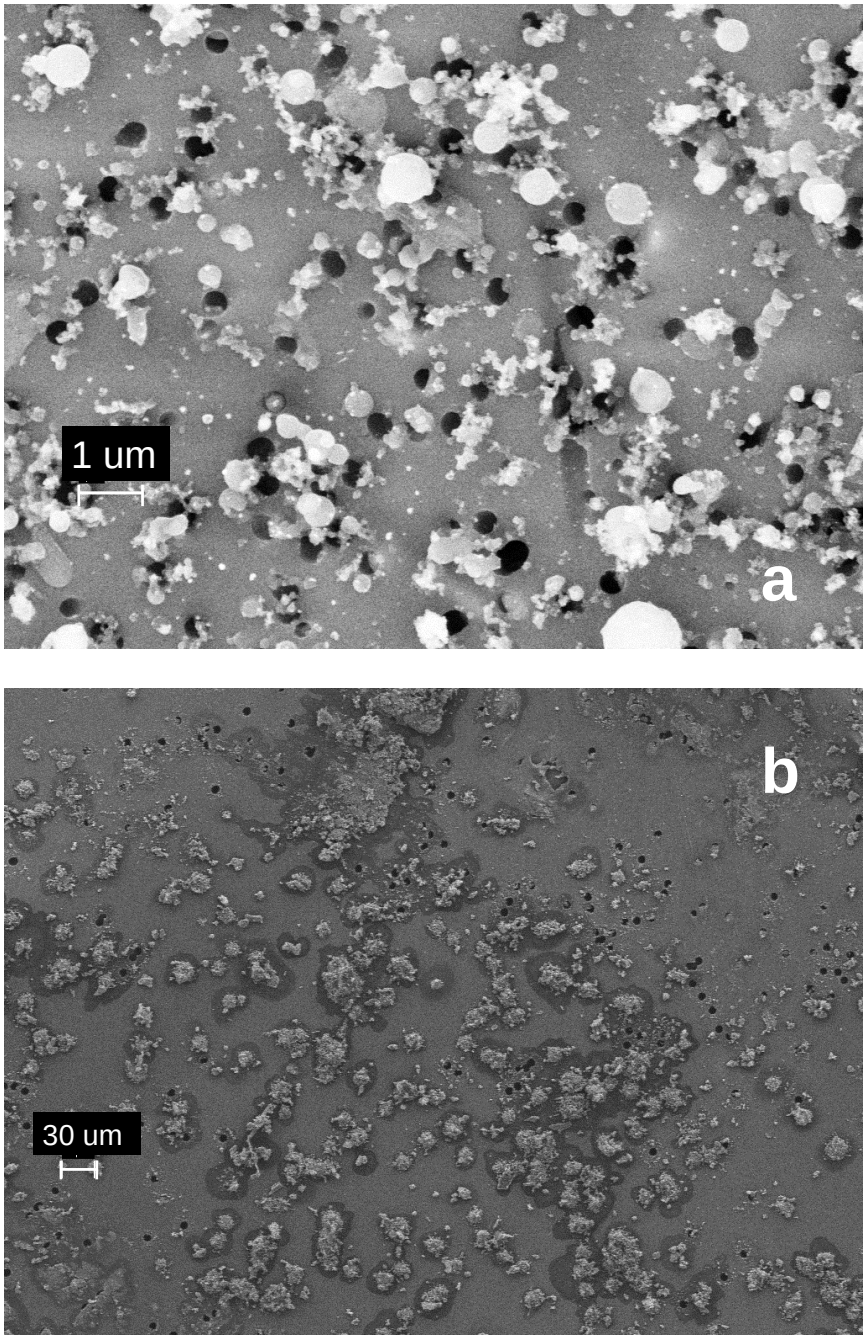

Figure 2.6: Scanning Electron Microscope image of a) March 10, 2005 fine mode filter and b) March 12, 2005 coarse mode filter.
The scale in figure a corresponds to 1 μm and the scale in figure b corresponds to 30 μm. The black circles shown are the filter pores whereas the particles are shown in white and gray tones.

2.3.2 Optical Properties compared to other ground-based instruments

The absorption coefficient calculated from a combination of the OR and the gravimetric mass concentration was compared to the University of Maryland's PSAP

instrument, which was run in parallel with the filter sampling apparatus during the IOC. Figure 2.7 shows that there is a better agreement between the two experimental techniques at lower values of the absorption coefficient, while the disparity between the data points widens at higher values, probably due to biases of the PSAP corrections for higher loading, and the excessive light attenuation allowed for those cases, which could have produced transmittances down to 60% (Figure 2.7b). At seven points the difference between the two measurements is greater than ±1E-05. The points where the OR measures a significantly greater absorption coefficient (March 7th, March 14th, and March 19th) were all during the night-time sampling period when the PSAP has difficulty taking continuous measurements (see below for discussion) (Figure 2.7a). The largest difference between points occurs over the whole day of March 16th ending on March 17th when there was heavy atmospheric loading.

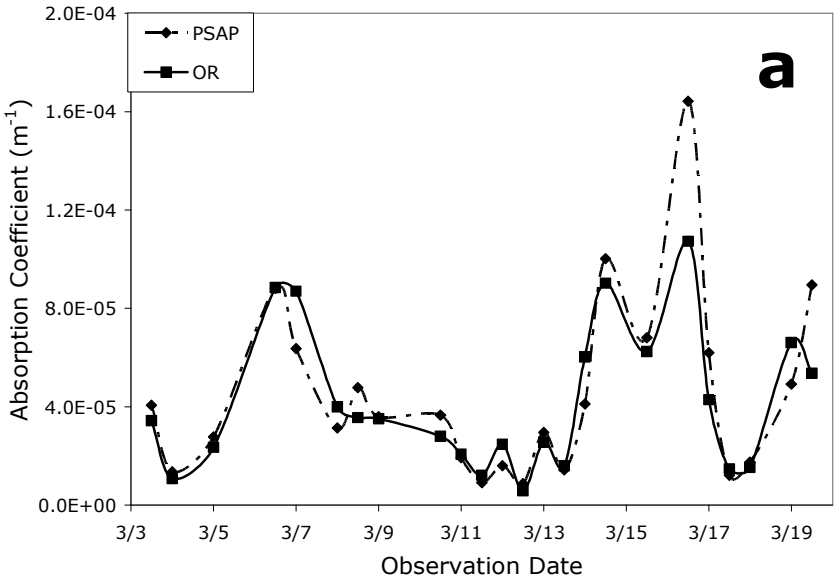

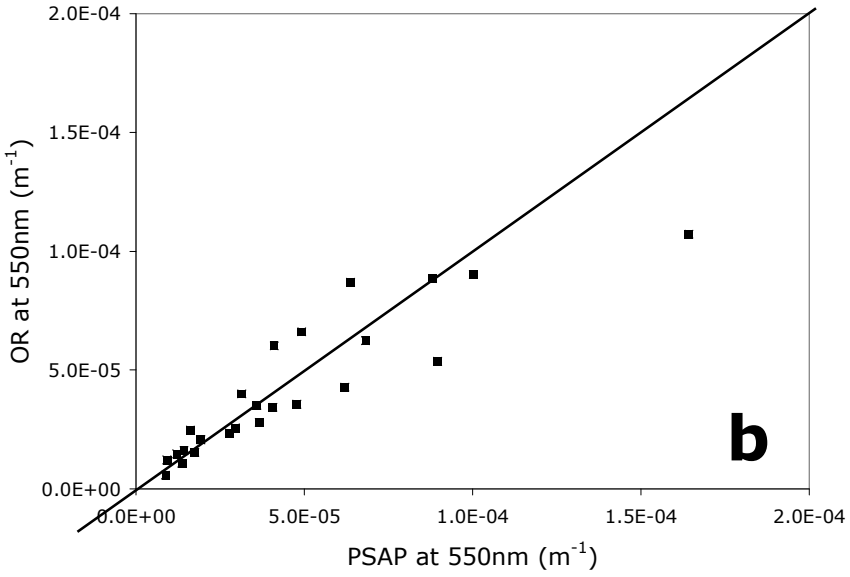

Figure 2.7: Comparison of absorption coefficient from the Optical Reflectance (OR) technique and the corresponding average PSAP results during the IOC.
Panel a depicts the time series of the absorption coefficient, while the two measurement techniques are correlated in panel b. A 1:1 line is shown for visual correlation.

Using the scattering coefficient from The University of Maryland's TSI 3-λ Nephelometer, the SSA (ω_0) was calculated for both the OR and the PSAP results. The absorption coefficient can be derived from the OR measurement at any wavelength from 350-2500 μm, but the Nephelometer only measures β_{scat} at 450, 550 and 700 nm. The ω_0 was calculated at these three wavelengths and is shown in Figure 2.8a as a time series. The single scattering albedo stayed above 0.8 until March 11th, when it fell below that level for a few days, only coming back above 0.8 on March 14th. The presence of strongly absorbing aerosols at Xianghe keeps the single scattering albedo mostly in the "cooling" regime (<0.85) [*Ramanathan et al.*, 2001a]. The spectral dependence of the single scattering albedo can be seen in Figure 2.8b, where the average ω_0 at 450 nm is 0.826, at 550 nm is 0.822 and at 700 nm is 0.796. The spectral dependence of the SSA gives information on the aerosol type.

The decreasing SSA with wavelength indicates an industrial/urban aerosol or a biomass burning aerosol type [*Dubovik et al.*, 2002].

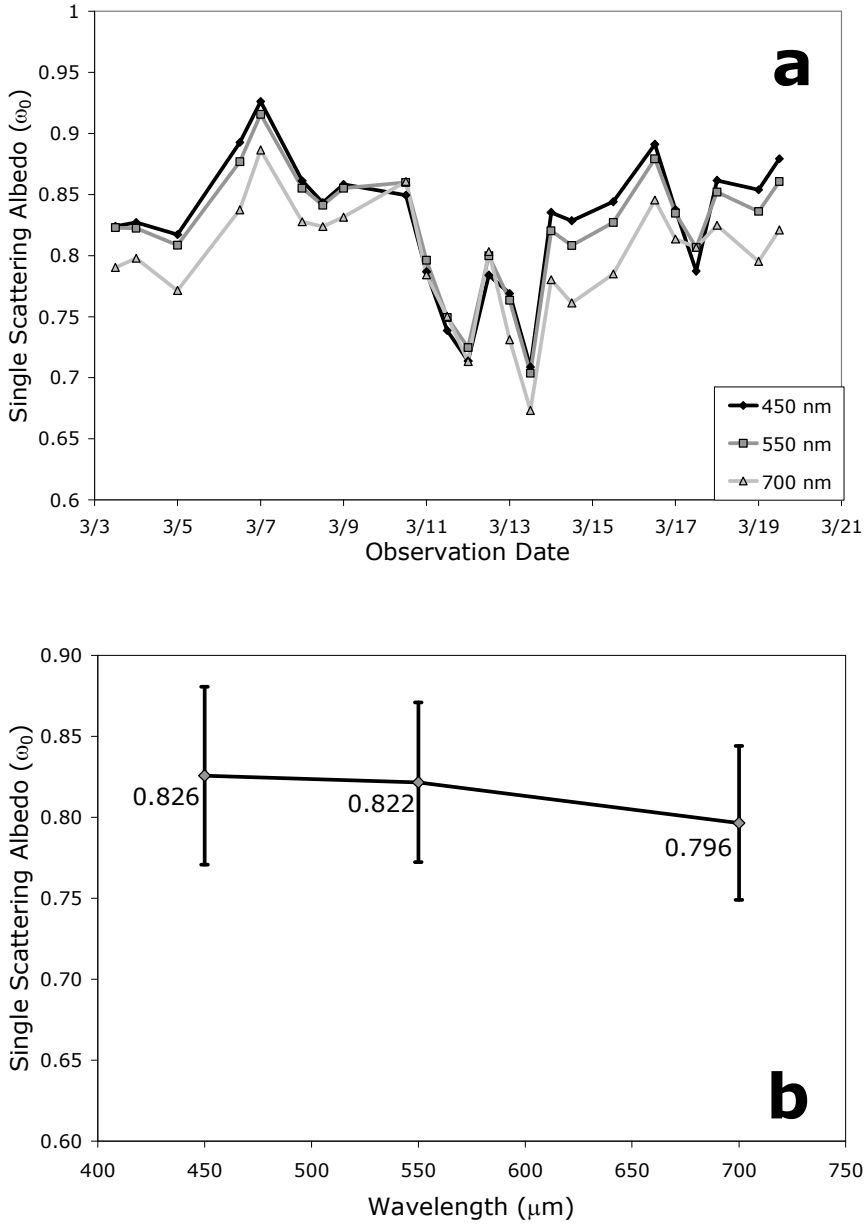

Figure 2.8: Single Scattering Albedo (ω_0) from Optical Reflectance combined with the Nephelometer scattering coefficient at the three operating wavelengths: 450, 550, 700 nm. Panel a depicts the time series during the IOC, while panel b shows the spectral dependence of ω_0.

Going from ground-based optical measurements to total column measurements, the OR ω_0 calculation at 550 nm is then compared with that from the

PSAP (extrapolated from 574 nm to 550 nm), and AERONET at 441 nm and 673 nm in Figure 2.9. The ω_0 from AERONET is an inversion product derived from almucantar and principle plane measurements, not direct sun measurements, and hence has fewer data points. To allow for some comparison, all data points during this time period are shown, not just daily averages. The data show that AERONET's ω_0 is higher than that obtained from the ground-based measurements. AERONET's inversion-based calculation would be influenced by aerosol layers aloft or possibly by hydration of the ambient aerosol particles, neither of which would affect the dry filter samples collected at the surface and analyzed in the lab. The range of ω_0 during the IOC is from 0.70 to 0.94, and the variation can be explained by the passage of cold fronts, wind direction and wind speed, as shown in *C. Li et al.*[2007].

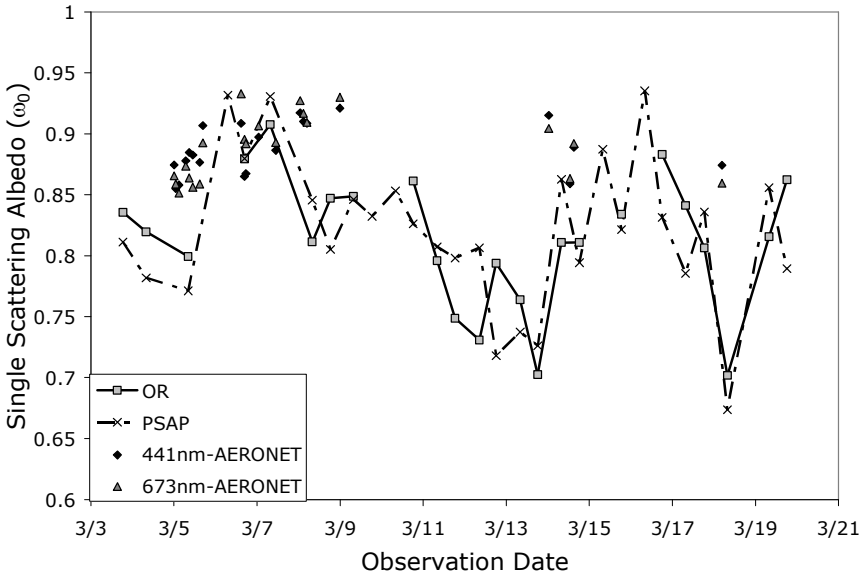

Figure 2.9: Single Scattering Albedo from AERONET and a combination of the scattering coefficient from the Nephelometer at 550 nm with Optical Reflectance and PSAP results.

Since the PSAP and Nephelometer instruments offer higher temporal resolution than OR, we examined the diurnal cycle of ω_0 to determine whether or not

the larger averaging time would impact the findings. In Figure 2.10, the daily cycle of ω_0 is shown with one standard deviation at each data point. Also plotted on the top is the number of data points that contributed to each average from the PSAP. Since the PSAP is a filter-based instrument using paper filters, the absorption measurement is only valid until a certain threshold of loading on the filter, at which time the filter must be replaced. In the case when an operator was not able to change the filter and the threshold was breached, those data were removed from the data set. The number of data points that contributed to each average point gives us an idea of the certainty of the measurement. The diurnal cycle of ω_0 shows two minimum values, one during the morning and one in the evening. The morning minimum occurs at a time when home heating systems are fired up and cooking for the day begins. Both minima can be attributed to rush hour commutes as well.

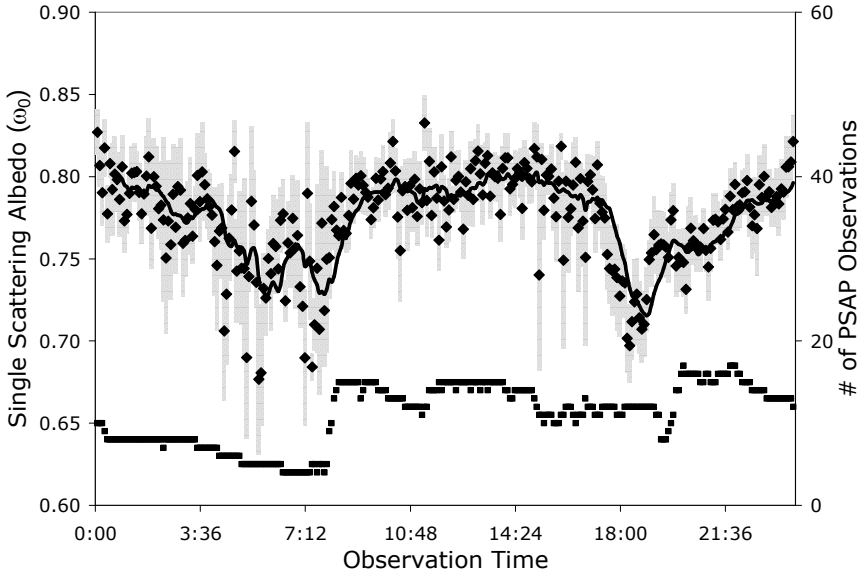

Figure 2.10: Diurnal cycle of Single Scattering Albedo from PSAP and Nephelometer (diamonds) with error bars (light gray) and the number of data points from PSAP contributing to the average (squares).

2.4 Physical Properties of aerosols during 2005

The mass concentration of the particles was determined by gravimetric technique, using the measured air volume sampled on each filter. The full year data record is shown in the eight panels of Figure 2.11. Each panel contains between one and two months of data, depending on the quantity of data available. For the 2005 calendar year, at least one filter was collected on 300 of the 365 possible days. During the IOC (panel c), filters were collected twice per day, one during daytime and one over night. Over the course of the year, the fine mode mass concentration ranged from 10 $\mu g/m^3$ to 244 $\mu g/m^3$, with an average of 44 ± 41 $\mu g/m^3$. The coarse mode mass concentration ranged from 12 $\mu g/m^3$ to 458 $\mu g/m^3$ with an average of 136 ± 101 $\mu g/m^3$. Both the wide range of values and the large standard deviations give an indication of the variability of the mass concentration.

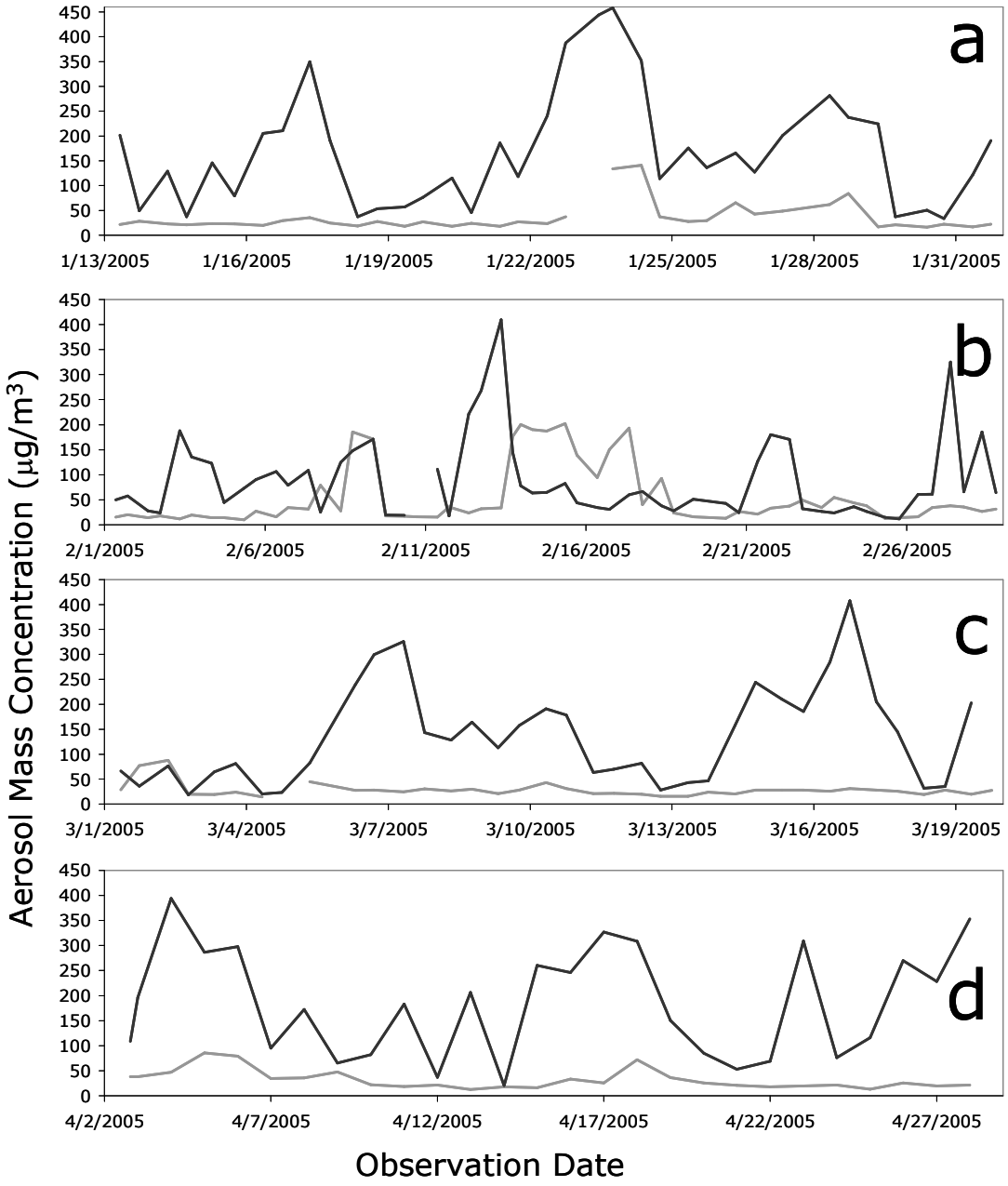

Figure 2.11a, b, c, d: Aerosol Mass concentration from Nuclepore filter gravimetry for the 2005 calendar year at Xianghe, China.
The black line is the coarse mode mass concentration, while the gray line depicts the fine mode mass concentration.

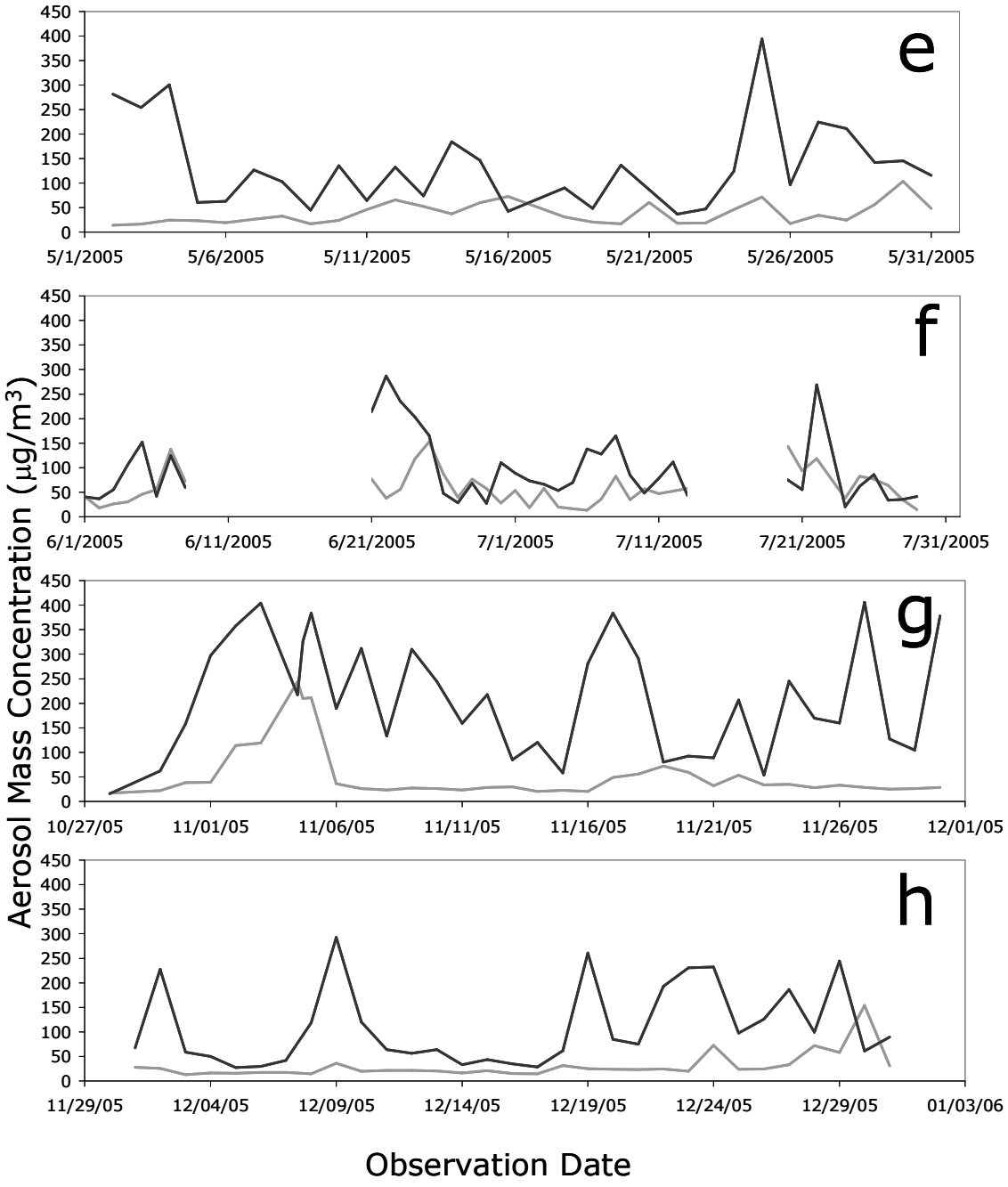

Figure 2.11e, f, g, h: Aerosol mass concentration from Nuclepore filter gravimetry for the 2005 calendar year at Xianghe, China.
The black line is the coarse mode mass concentration, while the gray line depicts the fine mode mass concentration.

This year of data can be deconstructed by closely examining the statistics by season (Table 2.1). The first column indicates the number of filters sampled during that season. Since filters were collected twice per day from January 2, 2005 through

the IOC to March 19th, 2005, there are more filters sampled during the winter and spring seasons. No filters were sampled during the months of August and September due to a supply shortage. Looking at just the fine mode, the lowest average mass concentration (32 μg/m^3) and the lowest maximum value (103 μg/m^3) were found in the spring season, during which the IOC took place. The highest seasonal average fine mode mass concentration is in the summer (59 μg/m^3). While the summer had the highest average, it also had one of the lower maximum mass concentrations at 153 μg/m^3, almost 40% less than the fall maximum (244 μg/m^3). This is explained in Figure 2.11f, where the fine mode mass concentration is higher overall, but with less fluctuation than in other seasons.

Table 2.1: Statistics of aerosol mass concentration by season during the 2005 sampling year.

	Days Sampled	Mean (μg/m^3)	1-σ Standard Deviation (μg/m^3)	Minimum mass concentration (μg/m^3)	Maximum mass concentration (μg/m^3)
Winter (Dec 2006, Jan/Feb 2005)	131				
Fine mode		43	46	10	202
Coarse mode		119	96	12	458
Spring (March, April, May 2005)	93				
Fine mode		32	19	13	103
Coarse mode		150	100	19	408
Summer (June, July 2005)	40				
Fine mode		59	36	13	153
Coarse mode		96	68	20	287
Fall (Oct, Nov 2005)	34				
Fine mode		55	58	16	244
Coarse mode		210	117	16	406

The coarse mode mass concentration has just as much variability between seasons as does the fine mode. The seasonal averages vary by a factor of 2, from 96 μg/m^3 in the summer to 210 μg/m^3 in the fall. The summer season has the lowest

average coarse mode mass concentration (96 $\mu g/m^3$), and the lowest maximum coarse mode mass concentration (287 $\mu g/m^3$). The highest maximum occurs in the winter (458 $\mu g/m^3$), which is almost twice the summer maximum measured mass concentration. The summer in Xianghe is the monsoon season, and the heavy rains wash out the large particles quickly and effectively. The cooler months are affected by dust storms and the increased emissions of soot from coal combustion during the heating season.

Aerosol mass concentration can be used similarly to aerosol optical depth to discuss atmospheric loading. Several studies have measured aerosol mass concentration in China, at different size intervals and time periods. *Bergin et al.*[2001] measured daily mean PM2.5 concentrations of 136 $\mu g/m^3$ with a standard deviation of 48 $\mu g/m^3$ during one week in June 1999 in Beijing, which expectedly shows higher concentrations than at Xianghe, a more suburban location. Also in Beijing, *Ning et al*. [1996] measured average total suspended particle (TSP) concentrations of 320 $\mu g/m^3$ in the summer and 680 $\mu g/m^3$ in the winter during two years of measurements in 1986 and 1987, which is consistent with the seasonal variation measured in this study. In another Chinese city, Shanghai, *Ye et al*. [2003] measured weekly PM2.5 mass concentrations ranging between 21 $\mu g/m^3$ and 147 $\mu g/m^3$ at two locations, with an annual average of 57.9 $\mu g/m^3$ and 61.4 $\mu g/m^3$ at each site, from March 1999 through February 2000. *Shi et al*. [2003] chose a suburban location, Nankou, a town 45 km northwest of central Beijing, to study mass concentration, similar to this study. The authors measured PM2.5 mass

concentrations of 177 ± 53 μg/m^3 and PM10 mass concentrations of 334 ± 96 μg/m^3 during one week in March of 2001.

2.5 Physical properties of aerosols during the 2005 IOC

During the IOC, filters were collected in 12-hour day and night samples, and a 24-hour average was calculated for PM2.5 and PM10. Here, PM10 is defined as the sum of the fine and coarse filter, which will account for all particles of d < 10 μm. The 24-hour IOC PM10 and PM2.5 results are shown in Figure 2.12. To put the data in perspective, they are compared with the US EPA National Ambient Air Quality Standards (NAAQS). The 24-hour average NAAQS limit, effective at the time of the IOC, for PM2.5 (35 μg/m^3) and for PM10 (150 μg/m^3) are shown in the plot. The PM2.5 limit was exceeded once during the IOC, at an average concentration of 35.4 μg/m^3 on March 10, 2005. The PM10 limit, however, was breached on 67% of the days of the IOC, and on those days averaged 47% greater concentrations than the NAAQS limit. While PM10 is considered to be a lesser health risk than PM2.5, the respiratory problems, visibility reduction, and weather and climate impacts that arise from high concentrations of PM10 are still valid concerns.

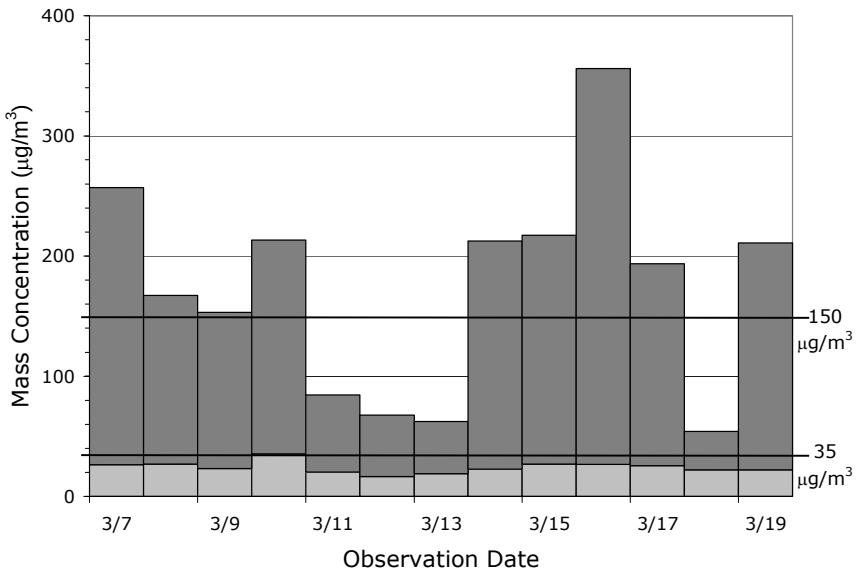

Figure 2.12: Twenty-four hour averages of PM2.5 (light gray) and PM10 (total column) during the IOC compared to the US NAAQS 24-hour limits for particulate matter.

In addressing the aerosol radiative forcing of the climate and health issues related to aerosol pollution, a major challenge remains as to how well the total column-mean properties of the aerosol retrieved from the ground (e.g. AERONET, *Holben et al*. [1998], *Smirnov et al*. [2000]) or from satellites (e.g. MODIS, *Kaufman et al*. [1997], *Remer et al*. [2002], *Ichoku et al*. [2002], *Chu et al*. [2002]) represent the mass concentration measurements or other observed aerosol properties at the ground level, or vice versa. The answer to this question has implications for the monitoring of aerosols from space and for the development of observation networks. The existence of aged versus fresh aerosol particles, or long-range transport of different aerosol types (e.g. dust transported over pollution aerosols), or the vertical distribution of relative humidity, or any other source of inhomogeneity in the vertical aerosol distribution throughout the atmospheric column can affect this relationship. This possibility must be studied in different locations and on a case-by-case basis.

One way to compare the ground-based filter measurements to total column remote sensing is to look at AERONET-based retrievals of aerosol particle size distribution. Note that the size distribution data from AERONET are derived from inversions of the almucantar and principal plane scans, while the direct sun measurement produces a quantity with less uncertainty, the Aerosol Optical Thickness (AOT). Due to the heavy aerosol loading at Xianghe, many more direct sun measurements were recorded than almucantar and principal planes as AERONET has difficulty distinguishing between heavy aerosol loading and cloud cover. Since the filter samples were collected in two size ranges, fine and coarse, a direct comparison of the Small Mode Ratio, SMR, can be performed between the filter results and the AERONET total column almucantar retrievals. The filter SMR is calculated by dividing the daytime fine mode mass concentration by the total (fine + coarse) daytime mass concentration. Only the daytime filters were selected, as AERONET can only collect data during daylight hours. The AERONET SMR comes from integrating the AERONET volume size distributions up to 2.24 µm diameter (the closest size bin constraint to 2.5 µm), and dividing by the total volume up to 10 µm diameter. The AERONET calculations assume the same mass density for the fine and coarse modes. Figure 2.13 shows a comparison between the SMR results of the filter versus AERONET. The 1:1 line indicated in the plot shows that there is one group of points with good agreement between both measurement techniques and a second group (circled) where the AERONET results show consistently larger SMR, indicating smaller particles in the atmospheric column than near the ground.

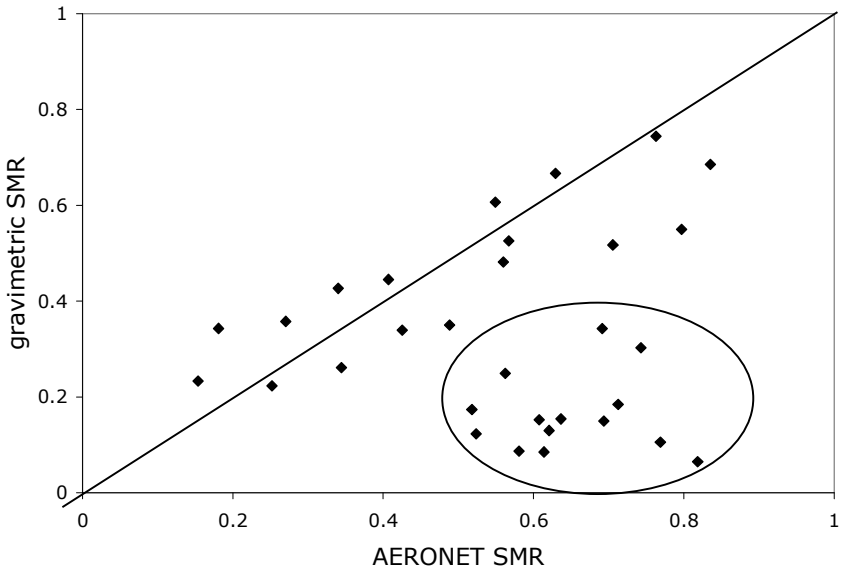

Figure 2.13: Comparison between calculated AERONET Small Mode Ratio and measured gravimetric Small Mode Ratio for available data from January 13-May 24, 2005. AERONET results were calculated from the average of almucantar inversions performed throughout the day, and the filter data was sampled during the daylight hours. The 1:1 line is shown in the plot to indicate cases of good agreement between both results. Cases of poorer agreement are circled.

For the circled data points, one would assume that there was an external factor that did not allow the ground-based measurements to accurately represent the total column, usually in the case of aerosol layers aloft or diurnal changes within a relatively calm boundary layer. To test this hypothesis, data were used from NASA's MPLnet, as a micro-pulse lidar was located nearby. Lidar scans for the dates with good agreement between the filter SMR and AERONET SMR showed relatively uniform aerosol concentrations throughout the measurable vertical extent, as shown by a representative scan in Figure 2.14a on March 13, 2005. The time-series of AOT from AERONET was laid over the corresponding scan time period to determine if lidar backscatter variations were related to aerosol loading, not cloud contamination or sampling biases in AERONET due to selective cloud cover during portions of the day. Lidar scans for dates with poor agreement between the SMRs usually showed

heavy aerosol layers aloft, or very inhomogeneous aerosol concentrations throughout the boundary layer, as seen in a representative scan in Figure 2.14b for one case on March 15 2005. Based on these results, we can say that the SMR data gathered by ground-based measurements are accurate representations of the total column in those instances when the total column is well-mixed.

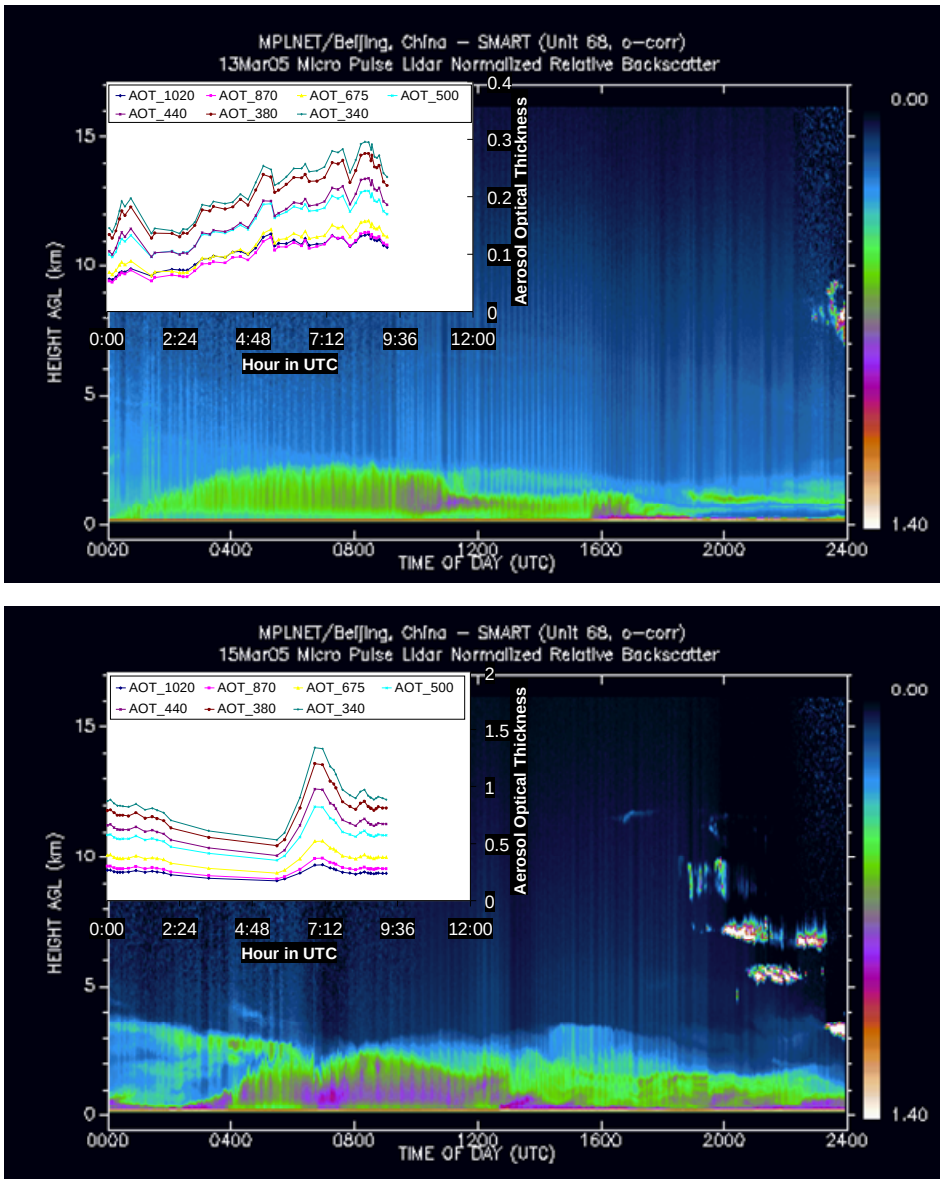

Figure 2.14: Lidar scan and corresponding AOD time series from AERONET for a) March 13, 2005, representing one case when the calculated AERONET Small Mode Ratio (SMR) and the filter SMR were correlated, and b) March 15, 2005, represents one case when the calculated AERONET SMR and the filter SMR did not correspond well.

Panel a shows a relatively well-mixed boundary layer during the AERONET data collection and the filter sampling period, while the lidar image in panel b shows significantly heterogeneous layers during the sampling period.

Assuming a constant mass extinction efficiency (m^2/g), one can determine how well the AOT retrieved by an AERONET sunphotometer can represent the mass concentration measured on the ground. *Smirnov et al*. [2000] offer a similar comparison from Barbados, studying transported Saharan dust. Only quality-assured AERONET level 2.0 daily averages from the sunphotometer located in Xianghe were used for this comparison. Since the sunphotometer computes AOT from its direct sun measurement, the daytime filters were selected instead of 24-hour filters, as the sunphotometer can only collect data during daylight hours. In Figure 2.15a, the fine mode mass concentration is compared to AERONET AOT at 500 nm, while Figure 2.15b shows a similar comparison with PM10 concentrations. With help from the SMR comparison, we can identify two distinct paths taken by the data. The points surrounded by circles in Figure 2.15a show cases where the correlation in SMR were poor, while points in squares indicate dates when there is no AERONET size distribution data available. This result serves as a guide to filter the best cases in the intercomparison between AOT retrievals and mass measurements. The resulting points (without the circled/squared points) present a better correlation between the AOT versus PM2.5 mass and provide a correlation coefficient of $R^2 = 0.84$, slope = 0.011 and intercept = -0.011. For the PM10 comparison, we present a correlation coefficient of $R^2 = 0.67$, slope = 0.0017 and intercept = 0.056. Comparable to this PM10 correlation, *Smirnov et al*. [2000] reported a correlation coefficient of $R^2 = 0.71$, slope = 0.0036 and intercept = 0.082 for daily filters from a high volume bulk sampler and daily average AOT measurements at 870 nm from AERONET of the

Saharan dust. They were able to improve the correlation to $R^2 = 0.93$ by presenting their 2.5-year data as one-month averages.

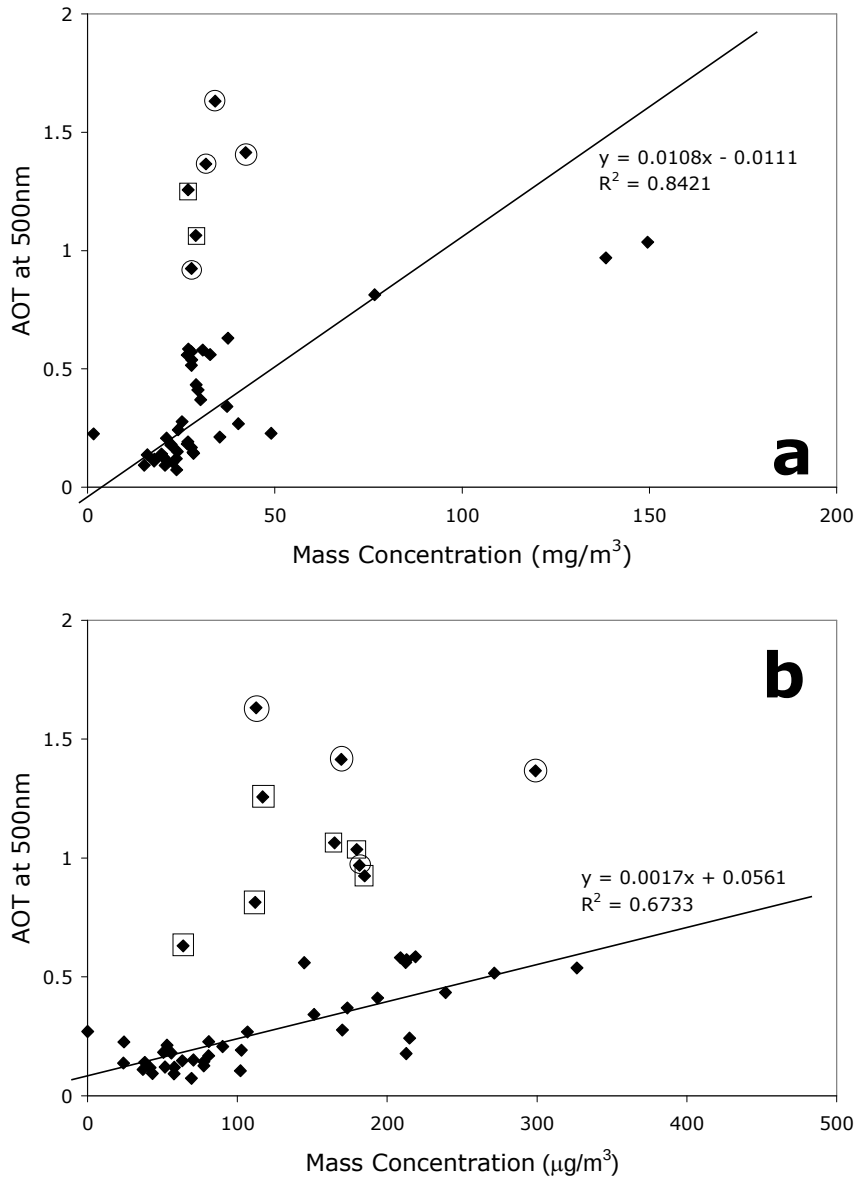

Figure 2.15: : a) Fine mode and b) PM10 concentrations versus AERONET AOT at 500 nm. The marked points are not included in the correlation; circled points indicate lack of agreement from the SMR comparison in Figure 2.13 while squared points indicate lack of AERONET size distribution data.

Chapter 3: Balloon-borne measurements of optical properties in China in 2008

3.1 Motivation

According to *Chaudhry et al.* [2007], ground-based measurements and total-column measurements are not equivalent, and more information is needed on where the aerosols are located in the atmospheric column to determine the climate impacts of aerosols. Vertical measurements are currently obtained from aircraft platforms, balloon-based platforms, and even kites. Each platform has its advantages and limitations. Aircraft platforms are readily available, with a wide altitude range. The drawbacks of aircraft platforms are the costs associated with instrumentation and flight hours, the limitations of aircraft inlet to pass coarse particles, and the meteorological conditions that limit aircraft movement. Balloon-borne platforms are simpler than aircraft platforms, allowing for more innovative instrumentation. Balloons can be tethered, where the altitude range is limited, or released, where the balloon can achieve a much higher altitude. One disadvantage of the balloon is that the payload capability available for instrumentation is much less than that of an aircraft. Meteorological conditions also affect balloon launches, with high wind conditions at the ground and aloft being the most problematic.

The layers of aerosols that form in the atmosphere have significant effects on the temperature profile, either by absorbing or scattering radiation that could affect cloud formation and inhibit pollution dispersion. Due to technical difficulties, there are very few measurements on the vertical distribution of aerosols in China [*Dickerson et al.*, 2007]. To this end, we have developed a balloon-borne Scattering-and-Absorption-Sonde (SAS). The instrument was developed at the University of

Maryland-Baltimore County's Department of Physics Laboratory for Aerosols, Clouds and Optics (UMBC-LACO) and was deployed in China in order to better understand the vertical distribution of aerosols, at lower altitudes than are currently obtained by lidar.

3.2 Instrument Design

The SAS is comprised of two major components: the Inverse Nephelometer, which measures scattering integrated over a large range of scattering angles (Figure 3.1), and the Reflectometer, which measures absorption with a similar technique to the one described in Section 2.1 (Figure 3.2). The particles enter the instrument through a curved copper inlet, designed to eliminate any stray light from entering the Nephelometer cavity. Following the inlet, the instrument has an impactor that cuts off particles larger than 10 μm with 50% efficiency prior to the Inverse Nephelometer [*Hopke et al*., 1997]. The light source for the scattering measurement is a class AA red laser, operating at 670 nm, housed behind the impactor so the particles flow around it. The laser beam is filtered by a series of collimators to refine and reduce stray light from the beam. Beyond the collimators is the scattering detector, a photomultiplier tube (PMT), which is housed perpendicular to the particle flow and the laser beam. As the particles cross the laser beam, the PMT detects the scattering of the laser beam by the particles. The location of the PMT gives it a wide field of view, such that both forward scattering (as the particles cross the laser beam with the laser behind them and the PMT in front) and back scattering (particles pass the PMT and cross the laser beam that is behind them) are measured. A cosine diffuser is placed in front of the PMT to integrate the phase function as a function of the

scattering angle. The laser beam continues to a cavity where a photodiode detector is located as a reference for any variation in the beam during a sampling period.

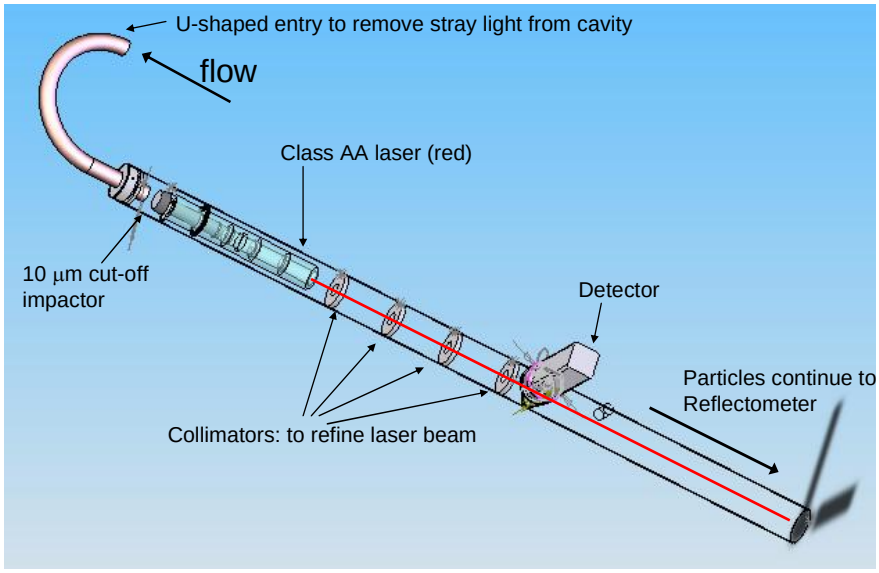

Figure 3.1: Schematic view of the Inverse Nephelometer design.

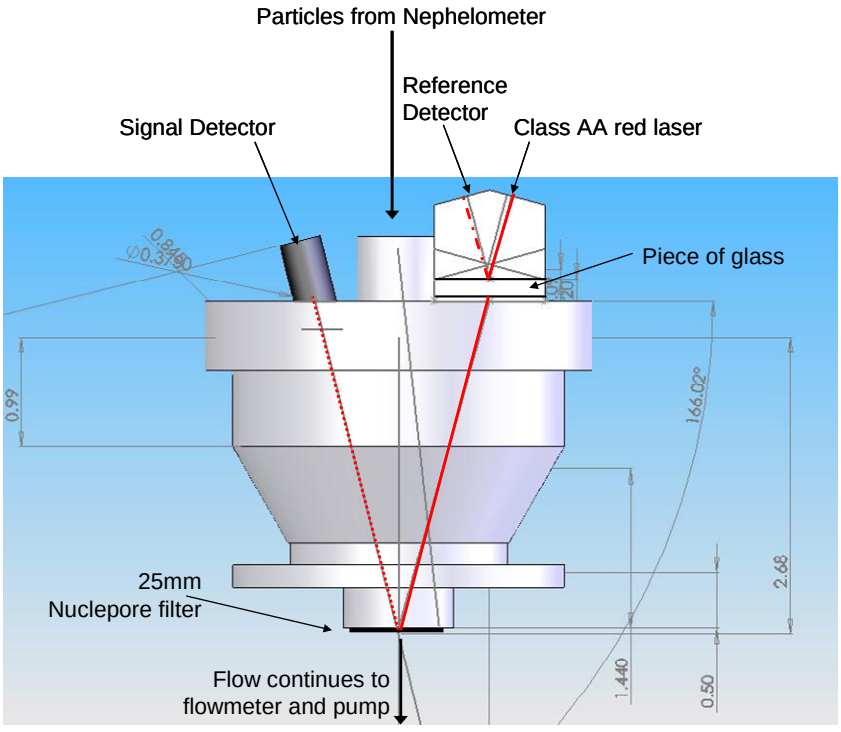

Figure 3.2: Schematic view of the Reflectometer design.

Scattering coefficients (β_{scat} in m^{-1}) were calculated from the raw PMT signal by correcting for the dark current, residual stray light and reference signal. The corrected signal was then converted to β_{scat} using the calibration curve from the pre-deployment calibration with N_2 and CO_2 at the University of Maryland-Baltimore County, where the instrument was designed, developed, built and tested. Rayleigh scattering was calculated for each launch, corrected for temperature and pressure. Rayleigh scattering was subtracted from the calculated β_{scat} to achieve aerosol β_{scat}. The data are presented here as 1-min running averages from the 1-sec measured β_{scat} to remove random instrumental noise.

The particles continue to the reflectometer (Figure 3.2), where particles collect on a 25 mm Nuclepore filter with 0.4 μm pore size. The reflectometer was designed following the OR technique described in Section 2.1. A class AA red photodiode laser, operating at 670 nm, was also used as the light source in the reflectometer. The laser beam passed through a tilted glass pane before striking the filter. Part of the beam was reflected off the top of the glass pane to a secondary detector, which acted as a reference for any variation in the laser beam. Under the filter were several substrates to provide mechanical support and enhance the reflectivity of the filter+substrate system, just as a Spectralon panel does for the OR technique in the laboratory. The primary detector measured the reflectance of the filter+substrate system after the beam was attenuated by particles on the filter. The attenuation was integrated over a 10 minute period to achieve the necessary signal reduction to calculate the absorption coefficient (β_{ap}). The filter was replaced for every balloon

flight, such that the sampled filters are available for any additional analysis (gravimetry, chemical composition, electron microscopy, etc.).

Based on pre-flight laboratory testing, we expected a sufficient signal reduction in the reflectometer over a 10 minute period to calculate the absorption efficiency. Unfortunately, many planned launches were shortened due to severe wind conditions. Since the instrument was not held at any one altitude for the 10 minute time period needed, it is difficult to vertically locate the calculated σ. For that reason, amongst other laser-induced problems, absorption efficiency profiles will not be included in this study.

3.3 Ground Validation

The SAS underwent extensive testing during the development stage at the UMBC-LACO. Prior to field deployment, the instrument was calibrated with N_2 and CO_2. Due to logistical issues, these gasses were not available after field deployment, and since the instrument was not recovered from the last launch, no post-field calibration was possible. All data have been corrected based on this pre-deployment calibration.

While gas calibration was not available, the instrument was run in Xianghe with a high-efficiency particulate air (HEPA) filter attached to the curved inlet. Since the HEPA filter removes 99.97% particles from the air prior to sampling, we expect a Rayleigh scattering signal similar to clean air. The Rayleigh scattering coefficient at 670 nm is 3.94E-5 m^{-1} for air at standard temperature and pressure, which becomes 3.69E-5 m^{-1} once it is corrected for temperature and pressure during the sampling period. The particle-free air produced an average scattering coefficient of 3.79E-5

m^{-1} on March 25th at Xianghe during one hour and 20 minutes of sampling, only 2.7% off from Rayleigh. This increases our confidence in the data as the HEPA filter cannot remove 100% of the particles, and the actual measured scattering is greater than the theoretical scattering coefficient for clean air.

The temperature-dependence of the detectors was tested throughout the deployment period. Before and after every launch or ground test, the dark current was measured by turning off the lasers for a short period of time. Since the temperature varied between the IAP laboratory in Beijing, field sampling in Xianghe, and field sampling in Zhangye, we were able to sample the dark current at a wide temperature range. It was determined that the dark current did not vary significantly with temperature, or with pressure, as the measurement site at Zhangye was at a much higher altitude than Xianghe, and the dark current remained the same.

In Zhangye, the COMMIT facility was operating a TSI 3-λ Nephelometer, which allowed for a ground-based intercomparison with the inverse nephelometer on the SAS. On April 19th, 2008, the SAS was placed on the roof of COMMIT and operated for approximately two hours while the TSI Nephelometer was operating. The TSI instrument was housed inside the trailer, while the inlet pulled flow off COMMIT's 10 m trailer inlet. Figure 3.3 shows the intercomparison between the total aerosol β_{scat} from the TSI instrument, corrected from 700 nm to 670 nm, and the calculated 5-minute running average aerosol β_{scat} from the SAS. Both instruments capture an increase in scattering during the first 30 minutes of sampling, and again during the last 15 minutes. In between these two periods of increased scattering, the TSI aerosol β_{scat} remains constant, while the SAS shows a decrease in aerosol β_{scat}.

This could be due to the higher sensitivity, faster response, and more frequent data recording of the SAS, or could be due to the instruments sampling different particles since the inlet for the TSI was 10 m above the placement of the SAS.

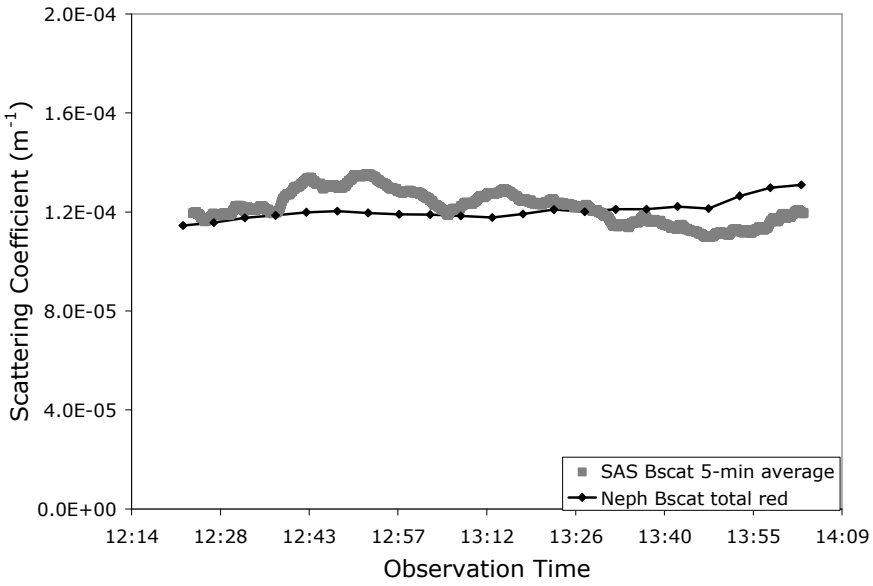

Figure 3.3: Ground-based intercomparison between Inverse Nephelometer on SAS and a co-located TSI 3-λ Nephelometer at the SAS operating wavelength of 670 nm.

3.4 Scattering Profiles

The SAS was launched together with a suite of sensors measuring pressure and temperature in China. The SAS was launched from March 19th - March 27th, 2008 at the Institute of Atmospheric Physics (IAP) facility in Xianghe (39.798° N, 116.958° E; 35 m above sea level), about 70 km ESE of Beijing (Figure 4.4). The measurement site was described in Section 2.2. The facility had access to hydrogen, which was used to fill the 10 m^3 tethered balloon. Hydrogen offers twice the lifting power of helium, but requires additional safety precautions. Launch conditions were in generally fair skies and light winds. Low wind speed was a requirement for the launch as the large size of the balloon and safety of launch personnel were at stake.

On the occasions when the wind speed was greater aloft than at the ground-level, the balloon would drift out of the property, and the length of the tether line had to be reduced as to keep the balloon within the IAP property boundary. As such, periods of light winds and fair skies usually came after a frontal passage, and for the time period available, the launch days had very low AOD.

Figure 3.4: Location of balloon launch sites in China.
The balloon was launched from March 19th-March 27th, 2008 at Xianghe, and from April 4th-April 26th, 2008 at Zhangye.

The first launch was on March 19th in the morning. The instrument was prepared with a new filter in a clean indoor environment prior to every launch. This first launch was a test to determine the maximum altitude achievable and to gauge an appropriate ascent rate. The balloon was held approximately 5 m off the ground to stabilize the reflectometer laser, protocol that was determined during pre-launch laboratory testing and followed for all launches.

The vertical profile of the scattering coefficient is plotted in Figure 3.5. In general, the β_{scat} measured in this profile was the highest of all the profiles. The ascent (shown in red) indicates a large amount of scattering aerosols, with aerosol layers at 1000 hPa and at 990 hPa. At the maximum altitude, the β_{scat} increases further, indicating the presence of another layer. On the descent, we see a smoother slope in the β_{scat}, with the exception of an increase around 995 hPa, where the 2 layers from the ascent may have merged into one layer. Through the rest of the descent, we note a lower β_{scat} than during the ascent, probably due to increased vertical mixing as the boundary layer height increased throughout the morning.

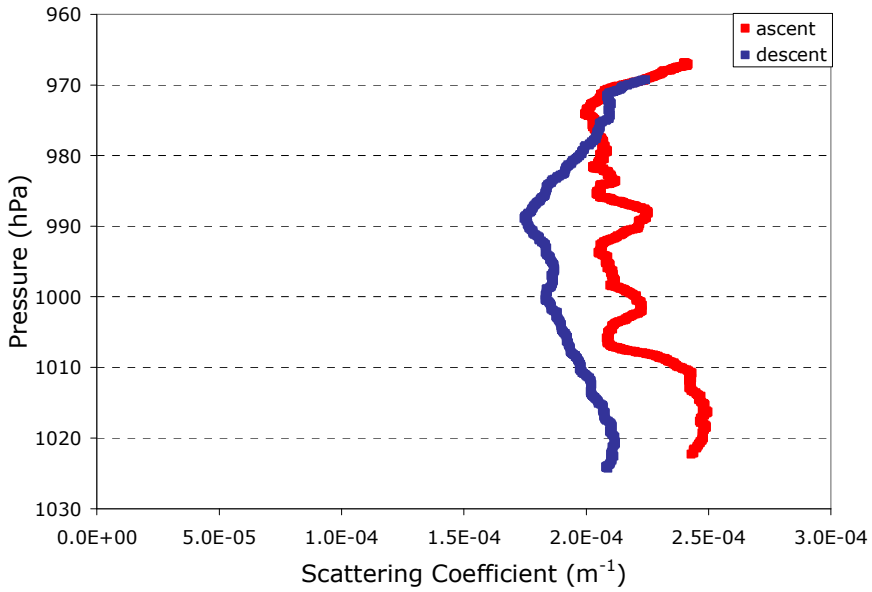

Figure 3.5: March 19th, 2008 morning launch at Xianghe facility.
Much higher scattering coefficient through out launch compared to other launches.

The second launch took place in the afternoon on March 19th, 2008. The wind speed had increased and we noted occasional wind gusts on the ground. Due to the strong winds, the instrument was launched to a lower altitude than during the morning launch. The ascent (shown in red in Figure 3.6) started with a moderate β_{scat}, but

decreased sharply, by almost half, within just 5 hPa of the surface, indicative of a very localized source of scattering aerosols at the ground level. The β_{scat} remained relatively low through the rest of the ascent. While the instrument was ascending, the balloon was caught in wind gusts that that influenced the balloon's direction. Occasionally, these involved vertical shear that caused the balloon (and instrument) to whip around "roller-coaster-like" loops. These loops can be seen in the β_{scat} during the descent at 980 and 990 hPa. The loops are seen in the vertical profile as the changes in altitude are recorded in the pressure measurement. The scattering detector itself is not influenced by the turbulence of the balloon, and continues to measure the ambient aerosol wherever it is.

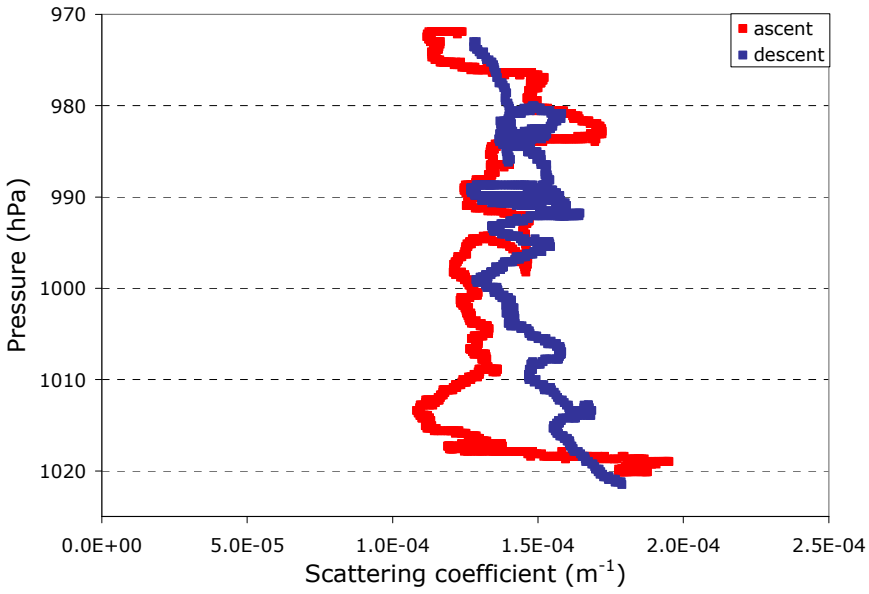

Figure 3.6: Scattering profile during March 19th, 2008 afternoon launch.
The scattering coefficient drops off steeply at the beginning of the ascent, indicating a strong scattering aerosol located at the surface.

We note a similar β_{scat} from 1000 hPa through the maximum altitude during the ascent and descent, but a higher β_{scat} during the descent from 1000 hPa to the surface. This could be due to local aerosol sources, such as unregulated, roadside

biomass burning, or a local factory. We note two aerosol layers between 1000 hPa and the surface during the descent, at 1008 hPa and at 1012 hPa, which could be these local plumes.

The third instrument launch was also at Xianghe, on March 26th in the afternoon. The balloon and instrument experienced violent turbulence during this flight, and the β_{scat} is almost indecipherable when plotted as a vertical profile against pressure (Figure 3.7 top). Looking at each leg of the launch as a vertical time series (Figure 3.7 bottom), however, the β_{scat} is very clear and proves that the scattering signal was not affected by the extreme turbulence of the launch. This profile measures a lower β_{scat} than the prior two launches. During the ascent, from 995 to 990 hPa, the β_{scat} indicates the presence of an aerosol layer that increases the β_{scat} above the low ground level. The descent of this launch was a difficult maneuver, as the balloon and instrument performed flips and dips like a roller-coaster.

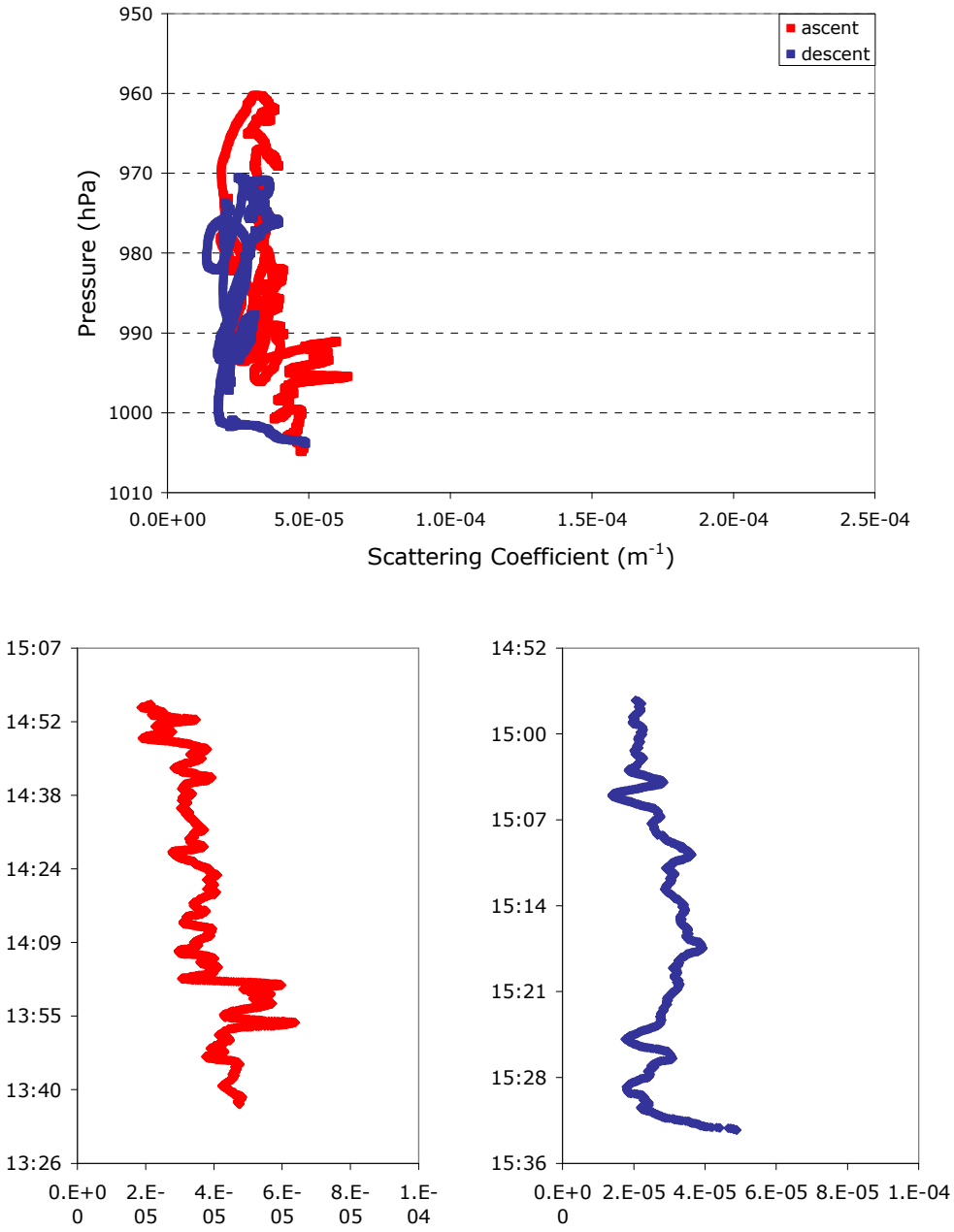

Figure 3.7: Scattering Profile for March 26th, 2008 afternoon.
The balloon experienced extreme turbulence, making the pressure-defined profile difficult to interpret. The bottom panels show the profile as a function of time, which shows the scattering sensor's stability in the face of turbulence.

The fourth instrument launch was performed the following morning, on March 27th, in Xianghe. The atmosphere conditions at launch time were clear skies, no clouds, and minimal winds. The ascent begins with a moderate level of aerosol

loading at the surface, followed by a steep decrease in β_{scat} all the way to 985 hPa (Figure 3.8). The β_{scat} remains at this low level through the rest of the ascent and through the whole descent. The lower ground-level β_{scat} from the descent shows how quickly the ground-level aerosol can get mixed into the atmosphere or dispersed out of the area.

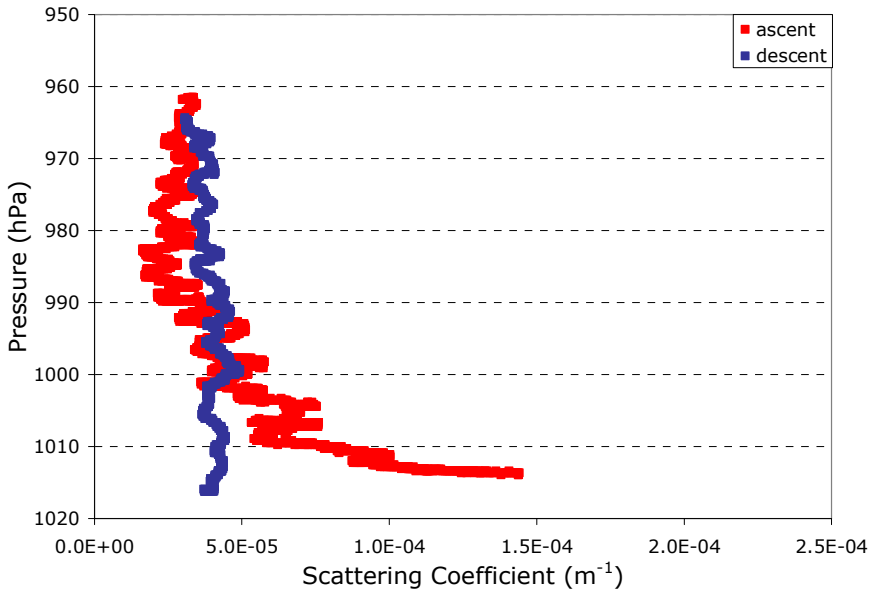

Figure 3.8: Scattering Profile from March 27th, 2008, morning launch.
The scattering coefficient drops off steeply soon after launch, similar to Figure 3.6. The strongly scattering aerosol is no longer present at the end of this launch as seen in the 3 times lower scattering coefficient.

The fifth instrument launch, and the last launch in Xianghe, took place in the afternoon of March 27th (Figure 3.9). The wind speed had increased from the morning launch time, but was still within the launch-limit, and far less than the wind speed from the 3rd launch. The conditions in the afternoon were a slightly hazy sky, light to moderate winds, and evidence of local aerosol sources (plumes from roadside biomass burning). The β_{scat} was low throughout the whole launch, but both legs of the profile resolve a layer of higher β_{scat} at 995 hPa.

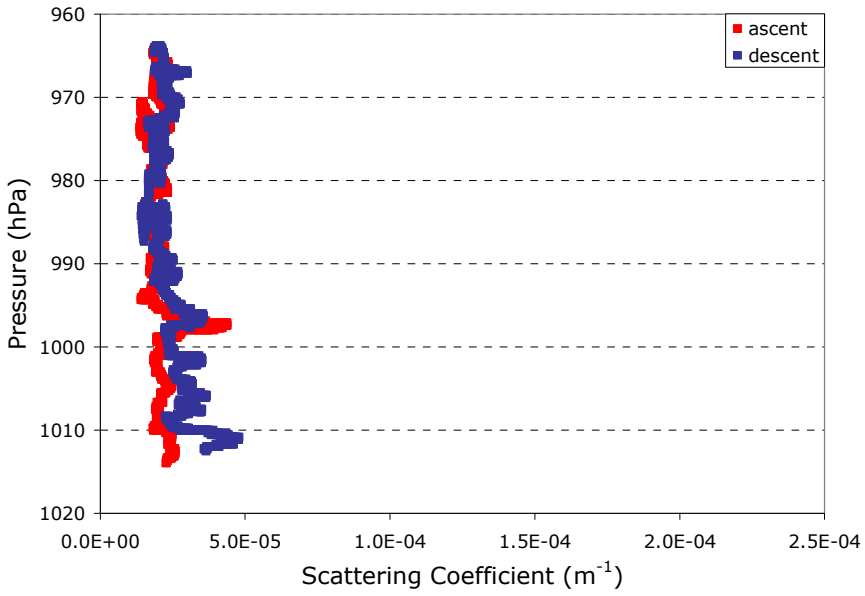

Figure 3.9: Scattering profile from an afternoon launch on March 27th, 2008. Both the ascent and descent have low scattering coefficients, but also both legs of the launch measure a layer at 995 hPa.

From April 4th-April 26th, 2008, the SAS was co-located with NASA's SMART and COMMIT trailers in Zhangye, China (Figure 3.4). Located in North-Central China, the semi-desert site at Zhangye (38.93° N, 100.58° E, 1483 m) is optimally located along the dust storm track between the Gobi and Taklamakan deserts and the heavily populated East Coast. With frequent dust storms, the high wind conditions allowed for only two short windows over the course of one month to launch the SAS.

The first launch in Zhangye took place on April 14th, 2008 (Figure 3.10). The launch began at 11:55am. The conditions were relatively calm, with haze visible on the horizon but a blue sky at the zenith. Thirty minutes into the launch, the balloon remained overhead but the tether line began to bow, a situation that happens when there is a windy layer between the surface and the balloon. After one hour of continuously ascending the balloon, the bowing got much deeper and the ascent was

stopped. The instrument was held for 10 minutes at 770 hPa, the maximum altitude reached. The return leg was slower than the ascent; it took almost 1 hour 20 minutes to return to the ground-level. The instrument and balloon reached the ground at 2:15 pm. While it appears that the ascent and descent scattering coefficients are not continuous at the maximum altitude in Figure 3.10, Figure 3.11 shows the β_{scat} measured while the instrument was held at the maximum altitude for 10 minutes, which declines smoothly to connect the two legs of the launch, from 1.0E-4 to 7.0E-5 m^{-1}. The vertical profile of β_{scat} showed remarkable differences between the two legs of the launch. The two layers in the ascent (at 840 hPa and 820 hPa) are almost a factor of two greater than the steady β_{scat} of the descent. This could be due to a wind shift that directed the aerosol plume away from the SAS.

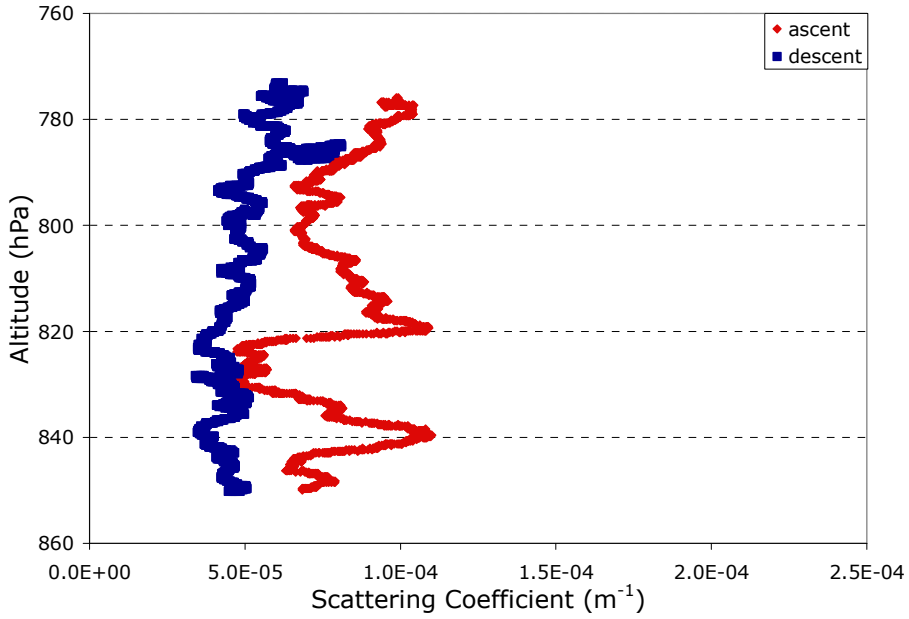

Figure 3.10: Scattering profile from a mid-day launch on April 14th, 2008 at Zhangye. Two layers are noted in the ascent, at 840 hPa and at 820 hPa, which are not as defined in the descent.

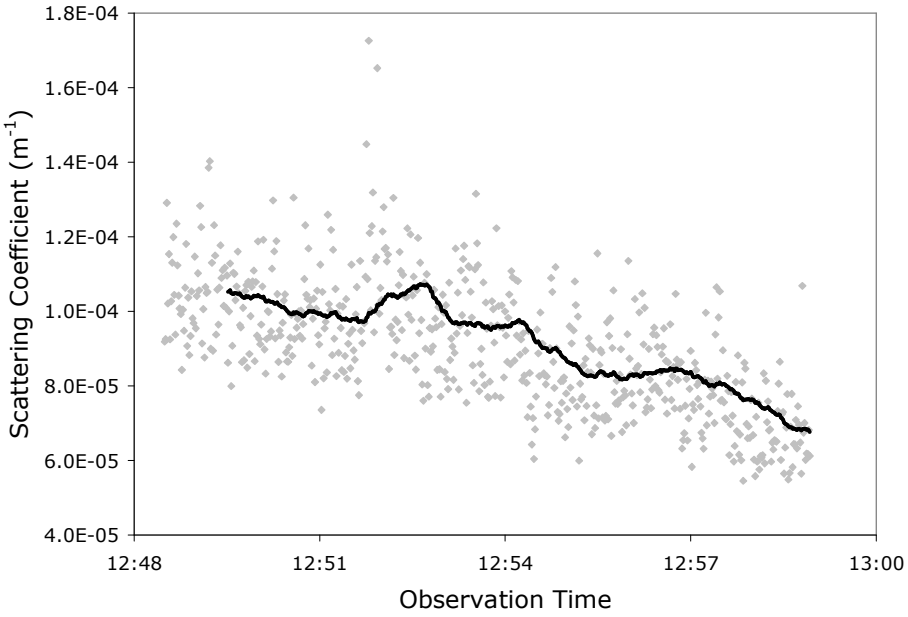

Figure 3.11: Scattering coefficient at the maximum altitude during the April 14th launch. The scattering coefficient smoothly declines from the top of the ascent to the beginning of the descent.

The next launch took place on April 21st. This was the latest launch performed, starting at 4 p.m., local time. The radiosonde was available and ready to use at this time. The SAS pump produced a vibration in the tether line that shook the radiosonde, so the two instruments could not be placed together on the line. The radio sonde was placed on the tether line about 5 m from the SAS. The radiosonde transmitted data in real-time to a laptop inside the COMMIT trailer, where an operator was communicating the instrument's position to the winch operator via hand-held walkie-talkies. The conditions were quite windy for this launch, so the balloon was raised quickly. At an altitude of 670 m above the surface, the force of the wind was very strong on the balloon, so the ascent was stopped. The instrument was brought back slowly, stopping at 500 m, 270 m, 120 m, and just above the ground, for 10 minutes each. The β_{scat} is noticeably higher in this profile than in the prior launch at Zhangye (Figure 3.12). There are numerous layers throughout the

column. The two legs of the launch measure similar aerosol layers at 838 hPa and 810 hPa, but are out-of-phase at 835 hPa and 820 hPa.

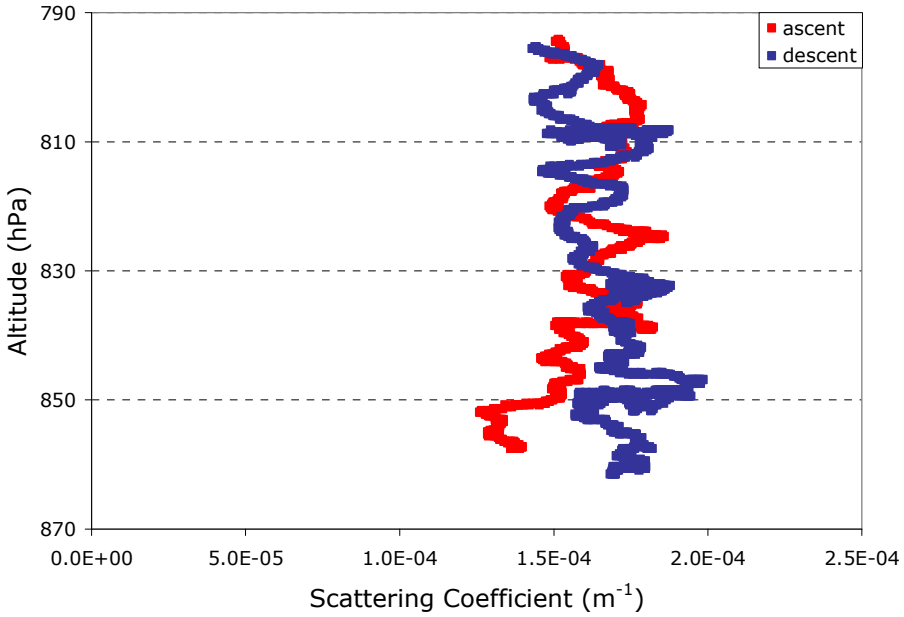

Figure 3.12: Scattering profile from the last launch, which took place on April 21st at Zhangye. The scattering coefficient increased as the balloon ascended and numerous layers are noted in both legs of the launch.

The final launch was attempted on April 23rd. Conditions on the ground were optimal for launching, light winds and a hazy sky. As the balloon was ascending, a layer of very strong wind aloft took over the balloon and flipped it around. The balloon was dangerously impacted by these winds, more so than during any previous launch. The decision was made to abort the launch. As the winch was reeling in the tether line, the balloon made a nose dive to the ground from about 200 m above. As it hit the ground, the tether line was cut by a gravestone in the nearby cemetery. The balloon and instrument, freed from the tether line, flew off, while the attached radiosonde was recovered.

Chapter 4: The Chinese Aerosol in a Global context

4.1 Motivation

The climate effects of aerosols vary on spatial scales from local to regional and even hemispheric effects. In this section, I examine how the aerosol physical and optical properties at Xianghe compare with aerosols from other urban locations. While China's growth in population and economy is unprecedented, other developing countries face similar problems of modernization and substantial emissions associated with a newly-mobile population.

Urban aerosols are formed primarily from anthropogenic sources (e.g., traffic, industrial processes, energy production, domestic and residential emissions, construction), but there is a minor contribution from natural sources (biogenic aerosols, soil dust, marine sources, volcanic ash, etc.). Once emitted into the atmosphere, this complex mixture of pollutants may be transformed as a function of the ambient conditions and the interaction among different aerosol components as well as gaseous pollutants. The urban aerosol is especially complex in mega-cities, due to large emissions of aerosol components and gaseous aerosol precursors, high variability of sources, widespread distribution of emission sources, and possible long-range transport of the polluted air mass [*Querol et al.,* 2008]. Monitoring air quality in large metropolitan areas is a pressing need in order to ensure the health and well-being of urban residents, but it is also essential if we intend to prevent air pollution-related problems from occurring in emerging mega-cities, which may influence both air quality and climate change on the regional, continental, and global scales.

Preventing pollution problems before they occur is usually the most cost-effective method for dealing with air pollution [*Molina et al.*, 2007].

The simplicity of the Nuclepore sampling train (Figure 2.1) allows for frequent deployment with little operator training. Over the last 10 years, Nuclepore filters have been collected in Xianghe, China; Bodele, Chad; the United Arab Emirates; Mexico City, Mexico; Zhangye, China; Sede Boker, Israel; Kanpur, India; Sao Paulo, Brazil; Wallops, Virginia; Cape Verde, Africa; and Thailand. To keep the comparison focused, I have chosen only those locations that exhibit a similar aerosol type to Xianghe, that of high atmospheric loading with influences of both pollution and dust. I selected Kanpur, India, and Mexico City, Mexico for this analysis.

4.2 EAST-AIRE IOC (2005) versus TIGERZ (2008)

The TIGERZ Campaign strived to characterize aerosols during the late pre-monsoon to early monsoon period in the Indo-Gangetic Plain in northern India. This region produces a large amount of anthropogenic pollution from urban, industrial and rural sources as well as dust from the Thar Desert and local sources. TIGERZ was primarily an AERONET campaign, with up to seven AERONET sunphotometers deployed around the major industrial city of Kanpur (26.51278° N, 80.23164° E, 123 m above sea level) (Figure 4.1). A filter sampling apparatus (installed at the India Institute of Technology, 17 km west of the center of Kanpur) was operated from May 21st to June 9th, 2008.

Other experiments to study optical, physical and chemical properties of aerosols in South Asia have taken place via cruise ships in the Arabian Sea/tropical Indian Ocean (INDOEX), and the Bay of Bengal (*Ganguly et al.*, 2005). The mission

of these ship-based experiments was to investigate how the natural marine aerosols interact with the continental outflow (*Ganguly et al.*, 2005) or to quantify the climate effects of haze over the Indian Ocean (*Ramanathan et al.*, 2001b) using multiple platforms.

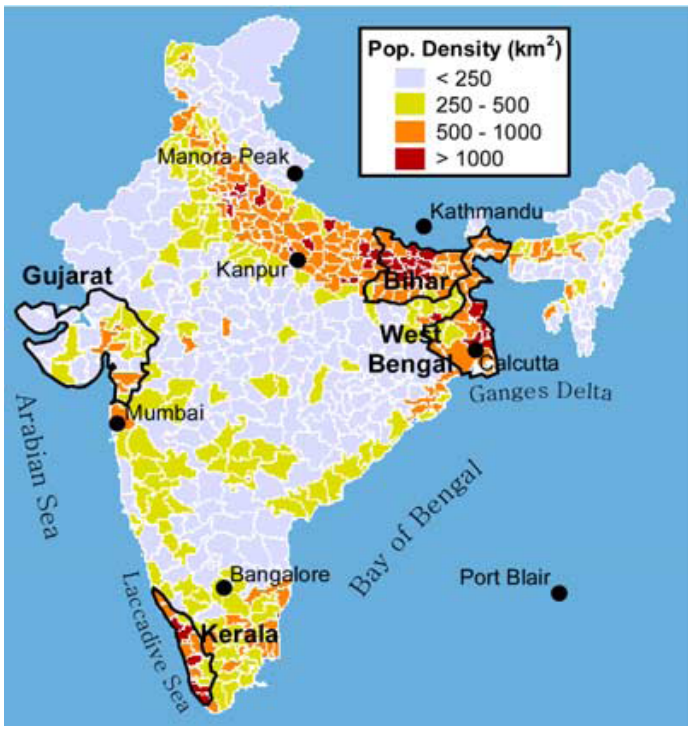

Figure 4.1: Location of measurement site (Kanpur) in India, shown with population density from 2001 Census data [*Di Girolamo et al.*, 2004].

The total coarse mode mass concentration (Figure 4.2a) shows a lot of variability in the atmospheric loading of these particles, with an average of 78 ± 42 $\mu g/m^3$ during the sampling period. Kanpur had much lower total coarse mode mass concentration than that measured at Xianghe during the 2005 IOC (149 ± 91$\mu g/m^3$) (Table 4.1). The total fine mode mass concentration (Figure 4.2b) shows less variability over the sampling period compared to the coarse mode, but also exhibits a higher frequency on a shorter temporal scale, with an average of 36 ± 9 $\mu g/m^3$ during

the sampling period. Compared to 24 ± 6 μg/m^3 at Xianghe during the 2005 IOC, the Kanpur site measured greater average fine mode mass concentration. The variability in the fine mode is the same at Xianghe and Kanpur.

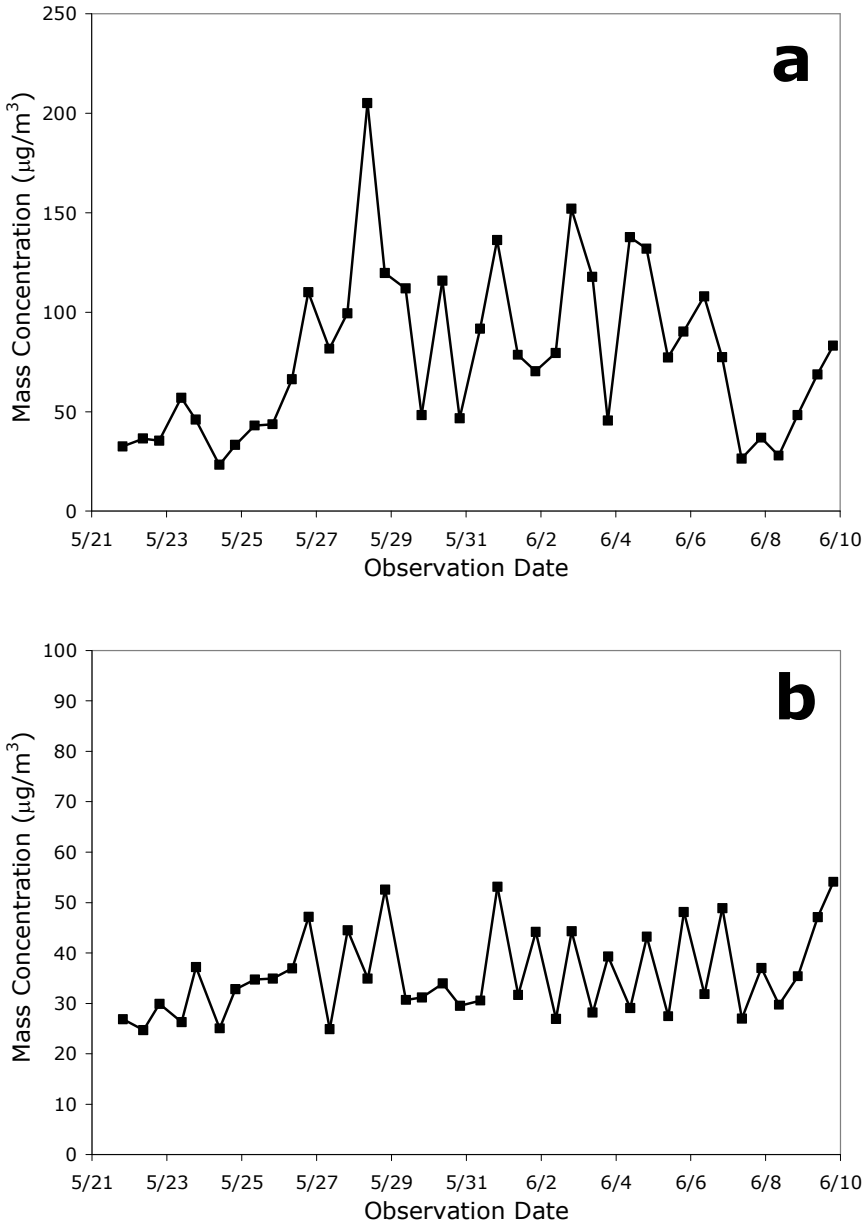

Figure 4.2: Aerosol mass concentration in the a) coarse mode and b) fine mode from May 21st 2008-June 9th 2008 at Kanpur, India.

Table 4.1: Fine and coarse mode mass concentrations from Xianghe, Kanpur, and Mexico City with the number of days of daily averaged size distribution data available from AERONET. The mass concentration is shown as a total value, from night and day sampling, and a daytime only value, to compare with AERONET sampling frequency.

	Fine mode mass concentration $\mu g/m^3$	Coarse mode mass concentration $\mu g/m^3$	# of days available for daily averaged size distribution from AERONET
Xianghe, China			19 days out of 25
total	24 ± 6	149 ± 91	
daytime	26 ± 4	158 ± 107	
Kanpur, India			4 days out of 21
total	36 ± 9	78 ± 42	
daytime	41 ± 8	74 ± 39	
Mexico City, Mexico			22 days out of 30
total	42 ± 14	61 ± 35	
daytime	47 ± 15	54 ± 21	

The diurnal cycle is readily apparent in the fine mode, especially from May 31st through June 9th (Figure 4.2b). The higher mass concentration is the daytime sampling period, indicating a surge in aerosol production during daylight hours, and a noticeable decline in ground level aerosol concentration overnight. This opposes the theory that ground level aerosol increases after the top of the boundary layer comes down and the aerosol are emitted into a smaller volume during the night. The increase of aerosol emissions during daylight hours overcomes this nighttime aerosol concentration to produce a greater ground-level mass concentration. This is especially harmful as the fine mode aerosol is inhalable and has been shown to cause respiratory illness [*Samet et al.*, 2000].

Babu et al. found that 53.6% of the total aerosol mass concentration in Bangalore in late fall 2001 is in the sub-micron size range [2002]. Their study used size-segregated surface aerosol measurements from a Quartz Crystal Microbalance Impactor. Bangalore, a mega-city with population 6.2 million and continental urban aerosol, was significantly less affected by dust events due to its southerly location compared to Kanpur. In our study, the fine mode comprises 34.8% of the total mass

concentration measured, indicating the stronger presence of coarse mode aerosols, which in this case are primarily dust.

Taking a look at the size distribution data from AERONET at Kanpur and Xianghe (Figure 4.3), Kanpur has a larger volumetric size distribution at the peak in both modes, and notably, a much larger volume of large particles compared to Xianghe. To compare this with the mass concentration, we look at only the daytime averaged mass concentration in the fine and coarse modes, to best correlate with AERONET's sampling period. Kanpur measuring greater volumetric size distribution than Xianghe is consistent with the daytime fine mode mass concentration comparison, as Kanpur measures 41 ± 8 $\mu g/m^3$ and Xianghe measures 26 ± 4 $\mu g/m^3$. However, this is the opposite of the conclusions from the coarse mode mass concentration, where Xianghe had the much higher daytime coarse mode mass concentration (Table 4.1). Since AERONET measures the total column of aerosols, one possibility for this discrepancy is that there was a substantial amount of coarse mode aerosols aloft during the sampling period, probably a plume of dust. Another explanation resides in the data used to make this comparison. As shown in Table 4.1, Kanpur only had 4 days, of the 21 days used in the mass concentration comparison, where daily averaged size distribution measurements from AERONET were available. Xianghe had 19 days of daily averaged size distribution measurements, out of a possible 25. The comparison of mass concentration to size distribution is less clear, as those 4 days from Kanpur may not be representative of the whole sampling period.

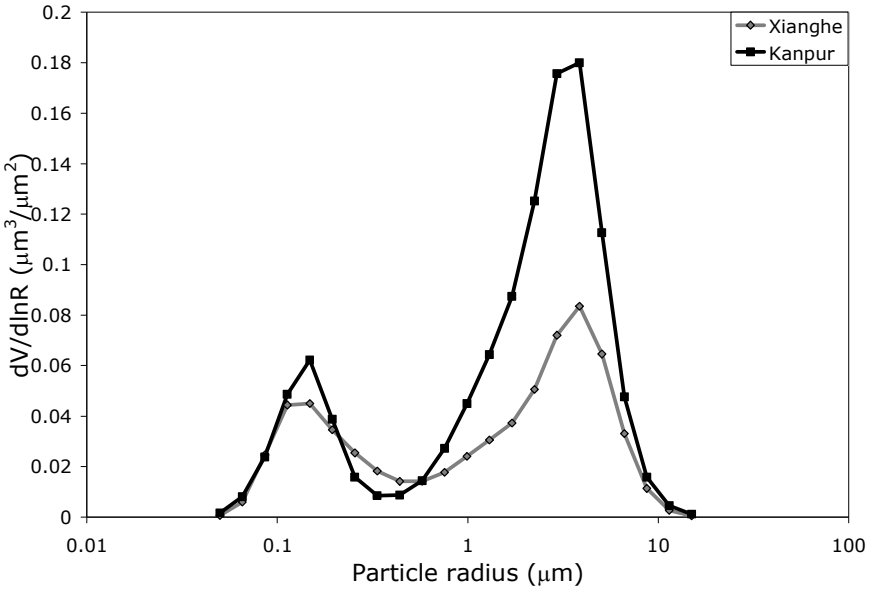

Figure 4.3: Volume size distribution from AERONET retrieval from the 2005 IOC at Xianghe (gray) and Kanpur, India (black).

The aerosol absorption efficiency (m^2/g) is shown in Figure 4.4a. The black curve is the fine mode absorption efficiency (standard deviation in gray), while the dark gray curve is the coarse mode absorption efficiency, with the standard deviation shown in black. Comparing the absorption efficiency in each mode to that at Xianghe (Figure 4.4b), we see that the absorption efficiency of both modes is higher in Xianghe. The fine mode spectra have a similar shape, while the coarse mode spectra do not. The Xianghe coarse mode is much flatter all the way to the shortest measured wavelengths, while Kanpur has some curvature. To compare the spectra in a more quantitative manner, Figure 4.5 shows the correlation between the two sites in each sampled mode. As determined qualitatively from the previous figure, these correlations concur with similarity between the fine mode particles and dissimilarity in the coarse mode. The correlation of 0.998 between the fine mode absorption efficiency in Xianghe and the fine mode absorption efficiency in Kanpur indicate the

presence of similarly composed and sized aerosols. This excellent correlation also indicates that the well-characterized fine-mode aerosol model from Xianghe may be used in radiative forcing calculations for Kanpur. In contrast, the correlation between the coarse modes' absorption efficiency is not as strong.

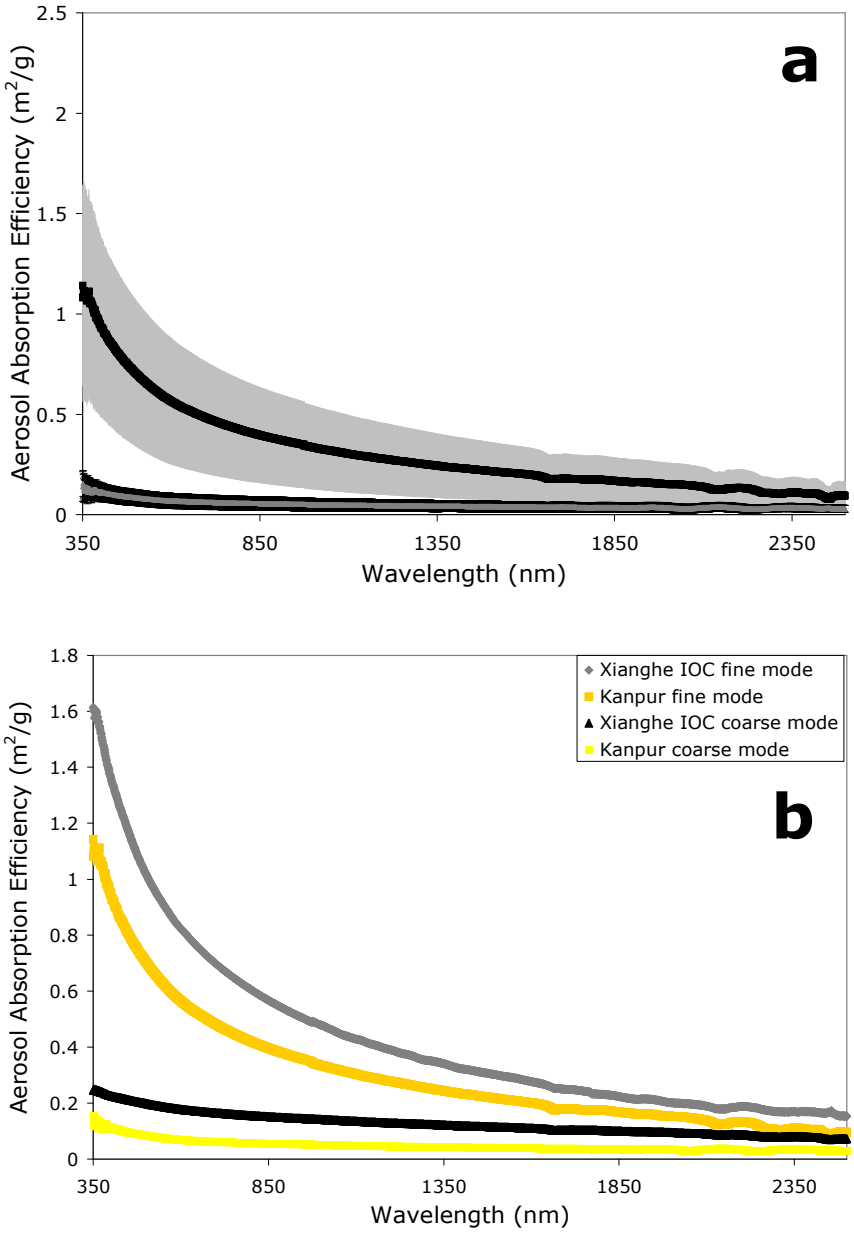

Figure 4.4: Aerosol Absorption Efficiency from Kanpur, India from May 21st, 2008 to June 9th, 2008.
Panel a) Fine and coarse mode aerosol absorption efficiency spectra with 1-σ shaded. Panel b) fine (orange line) and coarse mode (yellow line) from Kanpur plotted with fine (gray line) and

coarse mode (black line) from Xianghe IOC 2005. The absorption efficiency is greater in Xianghe for both measured modes.

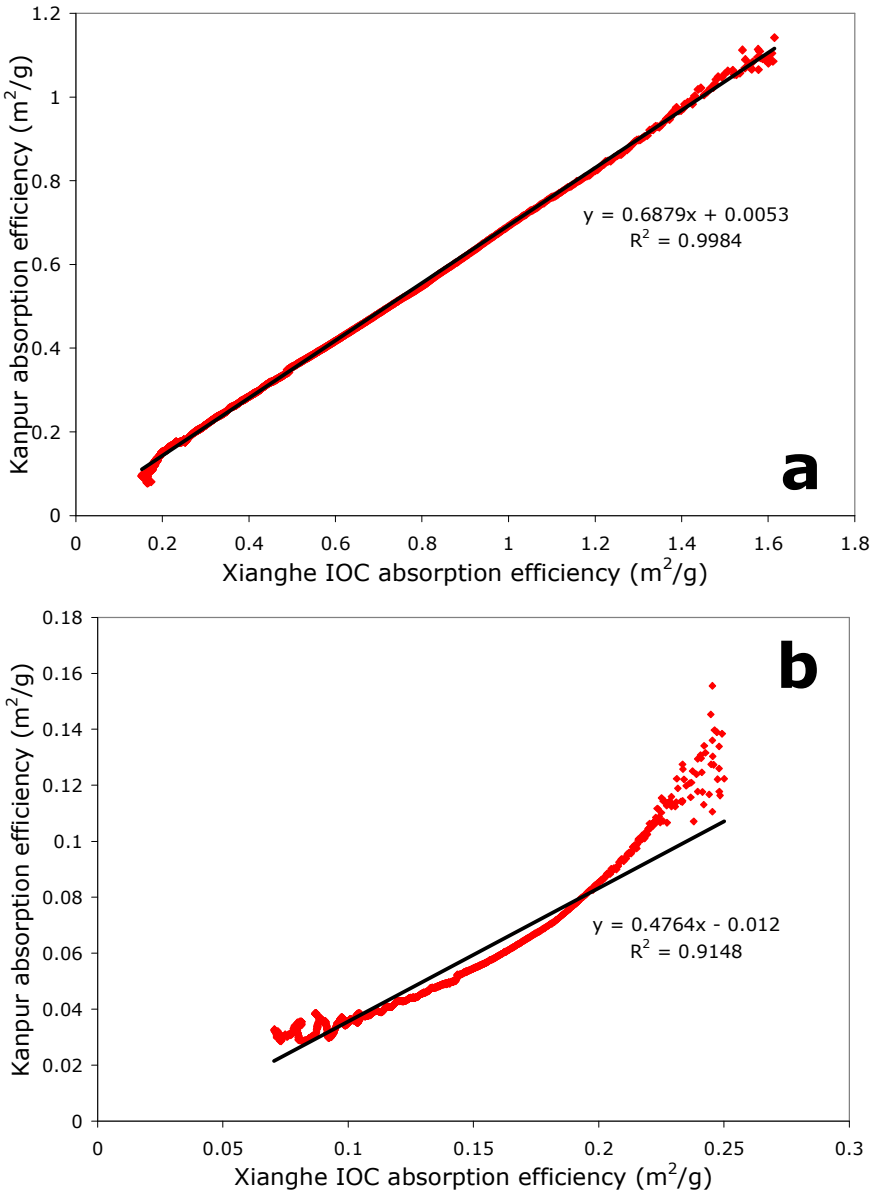

Figure 4.5: Direct comparison of Aerosol Absorption Efficiency at Xianghe, China and Kanpur, India.
The fine mode is shown in panel a, and coarse mode in panel b. The fine mode absorption efficiencies are very well correlated at an R^2 of 0.9984.

4.3 EAST-AIRE IOC (2005) versus MILAGRO (Mexico 2006)

The Mexico City metropolitan area (MCMA) is the largest urban center in North America and the second largest mega-city worldwide (second to Tokyo)

[*Molina and Molina*, 2002]. It occupies approximately 3540 km^2 with a population of about 19 million [*CAM*, 2002]. In general, megacities suffer from poor air quality due to the cumulative effects of rapid population growth and industrialization accompanied with increased traffic densities and greater energy consumption. The topography of the MCMA also acts to exacerbate the poor air quality, as Mexico City is located in a basin in the central Mexican plateau at an altitude of 2240 m and latitude of 19° N [*Fast et al.*, 2007, *Fast and Zhong*, 1998, *Doran et al.*, 1998]. The basin is surrounded on the south, east and west by mountain ranges that rise 1-3 km above the basin floor. This topography serves to inhibit dispersion of emissions within the basin during early morning hours and the high level of incoming solar radiation at this latitude and elevation promotes atmospheric photochemistry that rapidly forms secondary pollutants [*Whiteman et al.*, 2000].

In support of the over-arching MILAGRO campaign (Megacity Initiative: Local and Global Research Observations), Nuclepore filters were collected using the sampling apparatus (Figure 2.1) in three locations: the Instituto Mexicano del Petroleo in Distrito Federale (T0); at Racho la Bisnaga, outside Pachuca in the Hidalgo State, about 100 km NE of MCMA (T2); and at Tampico, which was about 300 km ENE of MCMA (Tam) (Figure 4.6). The topography of Mexico City allows pollution to build within the basin, until at some point the pollution is "washed out" of the basin. One component of MILAGRO involved studying this plume transport and characterizing the aerosol as it aged and traveled out of the region. The aerosol in the MCMA is a combination of vehicular exhaust, dust from nearby dust sources, and localized biomass burning. Data from T0 (Mexico City) will be presented here

for comparison to the Chinese aerosol, as the urban influence of the MCMA is seen most significantly in the T0 aerosol samples.

The sampling apparatus was installed on the roof of the Instituto Mexicano del Petroleo laboratories (Mexico, D.F.) co-located with numerous other instruments. The Instituto Mexicano del Petroleo is located in the north central part of Mexico City at latitude 19° 29' N, longitude 99° 09' W, and at an altitude of 2240 m above sea level. The IMP complex is a campus of 33 buildings located in an industrial and commercial area of Mexico City surrounded by streets that are very heavily trafficked by light duty vehicles and diesel buses. The nearest major roads are approximately 300 m away from the measurement platform.

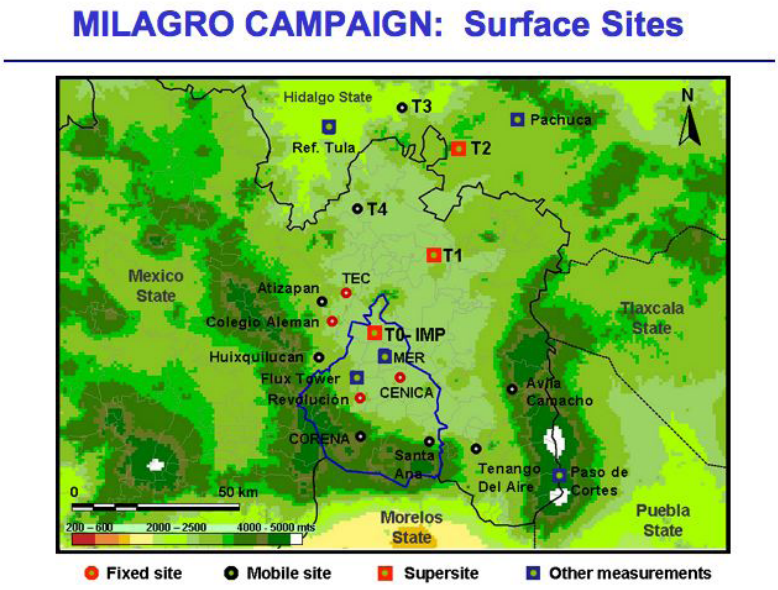

Figure 4.6: Location of measurement sites in Mexico City.

The basic sampling technique described in Section 2.1 was followed from March 7th, 2006 to March 28th, 2006. The aerosol loading was visibly high within the city limits, with poor visibility almost every day of the experiment. The total fine

mode mass concentration (Figure 4.7) averages 42 ± 14 μg/m^3 during the sampling period, almost twice the total average fine mode mass concentration measured in Xianghe during the 2005 IOC (24 ± 6 μg/m^3) (Table 4.1). The total coarse mode mass concentration is moderate, with a few episodic peaks, averaging 61 ± 35 μg/m^3 during the sampling period. This is almost one third of the total average coarse mode mass concentration measured at Xianghe during the 2005 IOC (149 ± 91μg/m^3).

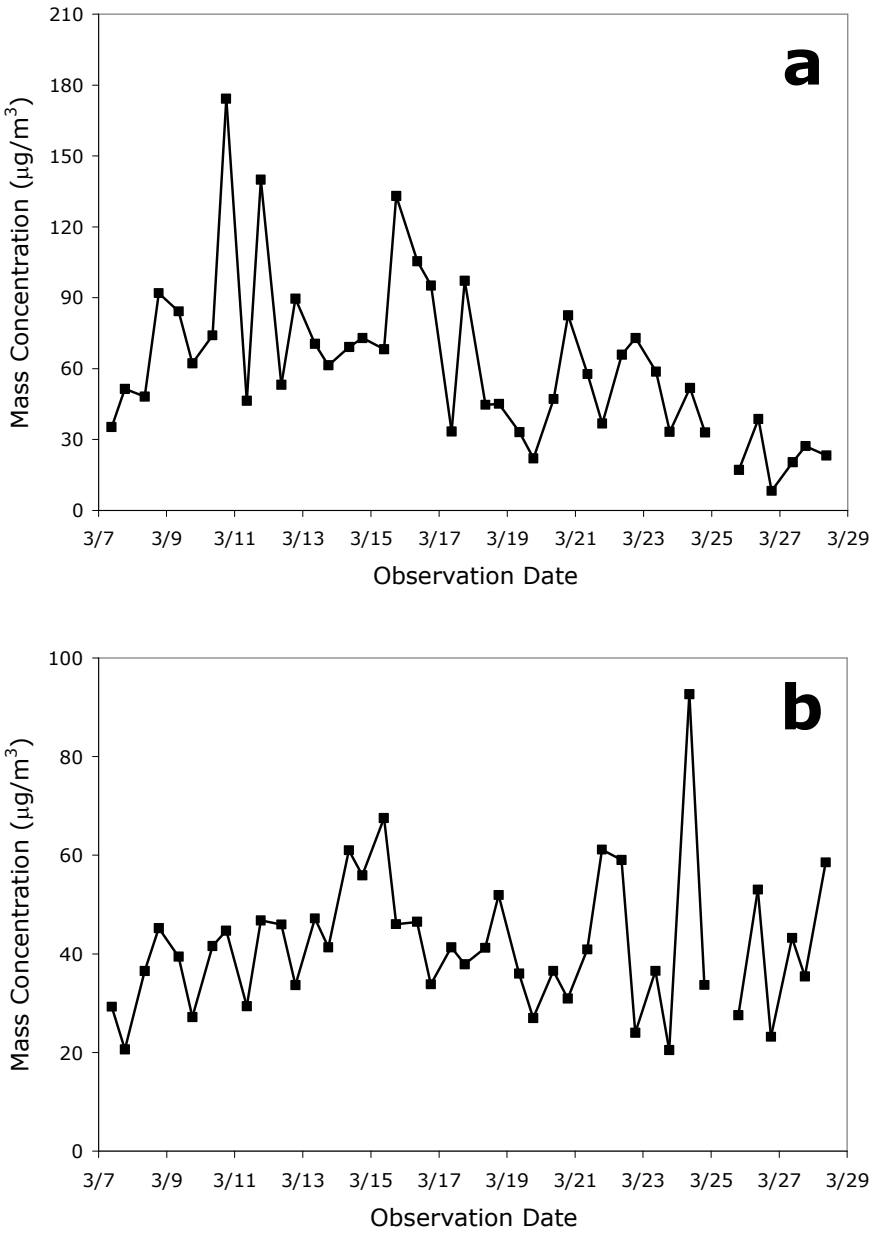

Figure 4.7: Aerosol Mass Concentration of the a) fine mode and b) coarse mode from March 7th-March 28th, 2006 in Mexico City.

Given these large differences between these two sites in the two measured modes, it stands to reason that the particle size distribution would follow the same pattern. AERONET sun photometers were operating at both locations during the respective campaigns. Volume aerosol size distribution data were obtained from AERONET's Version 2 Inversion Product as daily averages for the time period of

each campaign, and then averaged over the entire campaign (Table 4.1). The size distribution is compared to the average mass concentration of the fine and coarse modes derived from filters sampled during the daytime, as to best correlate with AERONET's sampling period (Table 4.1). The size distributions, shown in Figure 4.8, do not show a variation in the sampled modes at the same level as the daytime mass concentration measurements. We expect the daytime fine modes to differ by a factor of two with Mexico City measuring greater ground level mass concentration than Xianghe, but the size distribution in the fine modes at Xianghe is much greater than that at Mexico City when considering the total integrated volume below 2.5 μm. While the ground-level fine mode mass concentration was much greater at Mexico City, there might be additional fine mode aerosol aloft at Xianghe, resulting in a greater total-column size distribution. While the Xianghe coarse mode volumetric size distribution is greater than that measured at Mexico City, it is not larger by three-fold, as was measured in the daytime gravimetric analysis. In this case, Mexico City could have coarse mode particles aloft, perhaps a dust plume, which contribute to the total-column coarse mode volumetric particle distribution, but are not measurable from a ground-based sampling platform. The sampling frequency from AERONET is approximately the same for these two sites (Table 4.1).

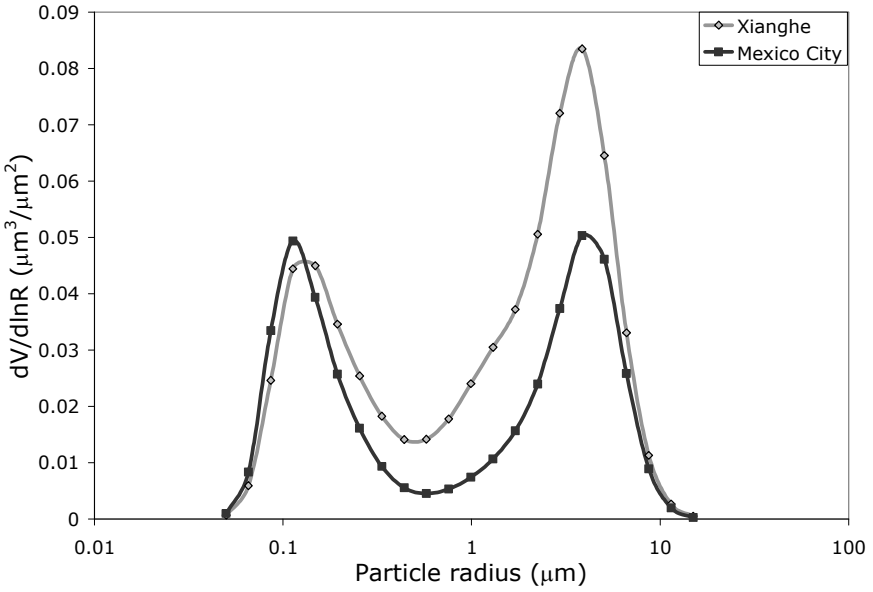

Figure 4.8: Volume size distribution from AERONET retrieval from the 2005 IOC at Xianghe (gray) and the MILAGRO campaign at Mexico City (black).

The fine and coarse mode absorption efficiencies are shown in Figure 4.9a. The fine mode follows the λ^{-1} curve well, while the coarse mode is generally flat. In comparing to the sampled modes at Xianghe (Figure 4.9b), we see that the fine mode absorption is greater at Mexico City than at Xianghe, and the coarse modes appear to be nearly identical. The fine mode spectrum from Mexico City has higher absorption than Xianghe throughout the whole spectrum, and has less curvature than the Xianghe spectrum. This dissimilarity can be seen in the scatter plot (Figure 4.10). The deviation from the linear fit in the short wavelengths suggests a different aerosol model. While the coarse mode absorption efficiency looked nearly identical between these two sites in Figure 4.9b, the scatter plot suggests otherwise. The correlation between the two sites is much better in this mode than that between Xianghe and India, but the deviation from the linear fit at shorter wavelengths suggests a difference in aerosol types.

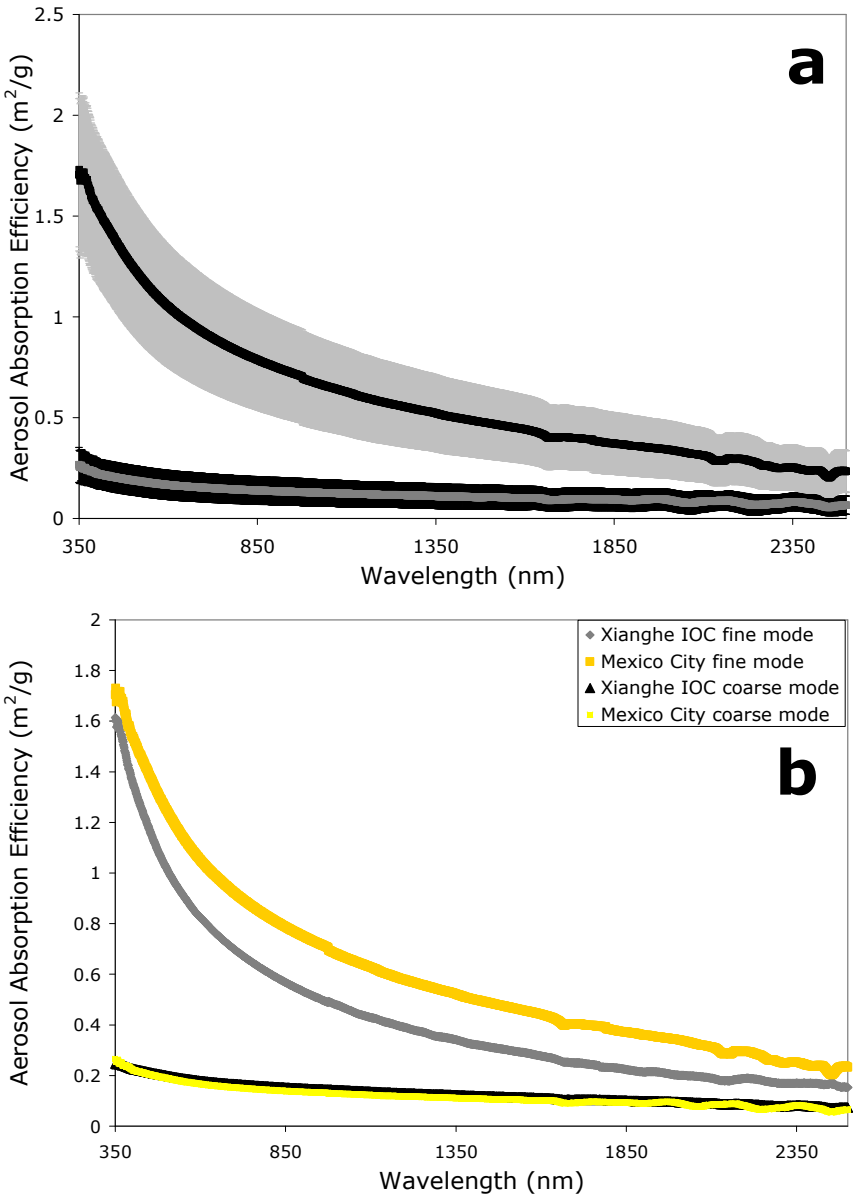

Figure 4.9: Aerosol absorption efficiency from (a) fine mode and coarse mode particles collected in Mexico City and (b) compared to the Aerosol absorption efficiency in Xianghe, China. The spectra of the fine modes have different curvatures, suggesting two different aerosol types at these two locations.

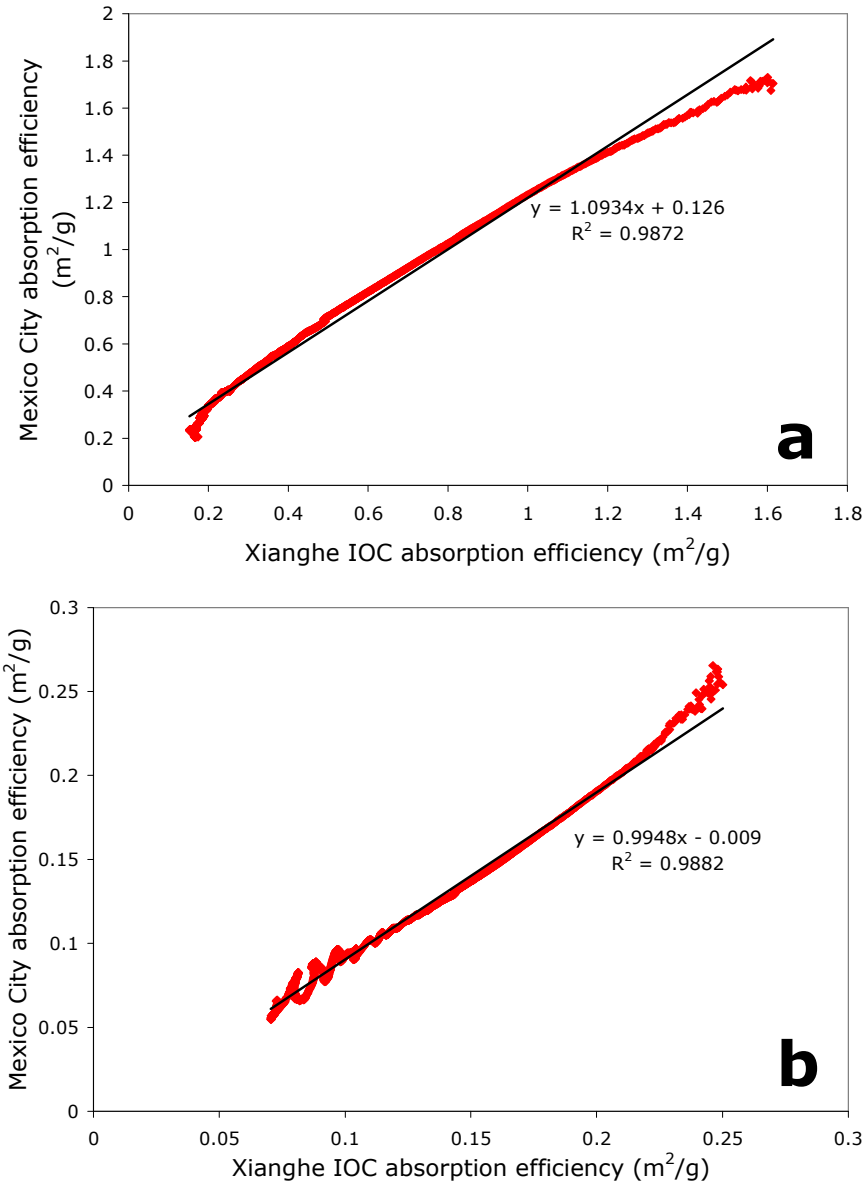

Figure 4.10: Direct comparison of aerosol absorption efficiency at Xianghe, China and Mexico City, Mexico in the a) fine mode and b) coarse mode.
The differences seen in the fine mode in the previous figure are more apparent here, with deviations from a linear fit at the shorter wavelengths indicating a different type of aerosol.

Chapter 5: Chemical Composition of Aerosol in Xianghe during EAST-AIRE 2005 IOC

5.1 Methodology

Elemental concentrations were obtained from the Nuclepore filters by PIXE (Particle Induced X-ray Emission) spectrometry. Twenty-seven filters from the IOC at Xianghe, China, from March 3rd-March 19th, 2005 were selected for this analysis due to the availability of co-located data during this time period. A 25 mm diameter circle was cut from the original 47 mm filters and mounted to a white plastic ring. The PIXE measurements were performed at the dedicated 5SDH tandem Pelletron accelerator facility of the University of Sao Paulo LAMFI (*Echalar et al.*, 1998). Concentration data were obtained for the following elements: Al, Si, P, S, Cl, K, Ca, Ti, Cr, Mn, Fe, Ni, Cu, Zn, Ga, Ge As, Br, Sr, Pb. Detection limits were typically 7 ng/m^3 for elements in the range $13 < Z < 22$ and 0.4 ng/m^3 for elements with $Z > 22$. These detection limits were calculated based on an average sampling flow rate of 16 lpm, sampling time of 12 hours and irradiation time of 600 s. The accuracy of the elemental concentration measurements by PIXE is typically better than 10% but degrades to 20% or more for elements with concentration near the detection limit.

PIXE spectrometry measures elemental concentrations by irradiating the sample with a high-energy proton beam (~2.5 MeV). The high-energy protons eject electrons from the innermost shells in atoms in the specimen. When that opening is filled by an electron from an outer shell, an X-ray quantum is emitted [*Johansson et al.*, 1995]. PIXE works best when the specimen targeted is thin, such that the accelerated protons lose only a small part of their energy when passing through the specimen [*Johansson et al*., 1995]. Thus, the excitation energy is well defined and

there is little absorption of the emitted X-rays in the specimen, simplifying the X-ray yield calculation. The Nuclepore filter is an excellent substrate for this analysis due to its thinness. The X-rays emitted from the irradiated sample are detected using a Si(Li) detector and produce an X-ray spectra with the characteristic energy of the photons from each element on the x-axis and "counts" on the y-axis. After a quantitative calibration, the elemental X-ray counts are converted to the mass of that particular element present in the sample.

5.2 Elemental Mass Concentration

The average mass concentrations of the elements are presented for the coarse mode (Table 5.1) and fine mode (Table 5.2) aerosols. In the coarse mode, the elemental mass concentration accounts for between 12.4% and 32.8%, with an average of 25.0% of the gravimetric mass being accounted for by the measured elemental mass concentration. The standard deviation of each elemental concentration is very high, and larger than the mean in the cases of S, Cl, K, Ni, Cu, Zn, Ga, Ge, As, Br, Sr, and Pb. This is indicative of the high natural variability of these elements at Xianghe.

Table 5.1: Statistics of coarse mode elemental concentrations in ng/m^3.

Elements	Mean (ng/m^3)	Standard Deviation (ng/m^3)
Al	4193.1	2579.5
Si	8935.5	5155.8
P	115.0	67.2
S	3740.7	5651.3
Cl	3341.8	3360.8
K	4120.5	8927.3
Ca	5419.9	3171.5
Ti	302.5	174.9
Cr	10.9	9.0
Mn	123.0	93.8
Fe	3765.7	2380.5
Ni	3.4	3.7
Cu	48.8	68.5
Zn	493.4	556.1
Ga	5.2	8.1
Ge	1.0	2.0
As	45.5	50.5
Br	14.6	20.3
Sr	30.9	61.8
Pb	233.6	246.2

Table 5.2: Statistics of fine mode elemental concentrations in ng/m^3.

Elements	Mean (ng/m^3)	Standard Deviation (ng/m^3)
Al	441.0	280.2
Si	1093.9	688.1
P	32.8	10.2
S	1142.4	543.3
Cl	295.6	163.2
K	684.0	308.3
Ca	541.3	305.2
Ti	31.9	19.0
Cr	1.0	2.3
Mn	23.7	9.9
Fe	410.4	235.9
Ni	0.7	1.1
Cu	10.6	11.3
Zn	106.4	75.2
Ga	2.0	1.4
Ge	0.7	1.1
As	13.1	9.5
Br	6.6	6.3
Sr	1.9	2.8
Pb	64.4	41.5

In the fine mode, the elemental mass concentration accounts for between 9.0% and 31.7%, with an average of 19.8% of the gravimetric mass being accounted for by the measured elemental mass concentration. The average elemental concentrations are much lower in the fine mode than in the coarse mode, which is expected due to the difference in mass. The standard deviation is much less in this mode as well, compared to the average. Only Ni, Cu, Ge, and Sr exhibit standard deviations greater than their averages.

5.3 Principal Component Analysis

A multivariate statistical technique, principal component analysis (PCA) [*Harman*, 1976; *Henry*, 1991], was used to identify the different sources that contribute to the atmospheric aerosol of Xianghe. In addition to the average elemental concentrations, the aerosol absorption efficiency at 3 wavelengths (360 nm, 550 nm, 660 nm), scattering coefficient at 550 nm from UMD's co-located 3-λ TSI Nephelometer, gravimetric mass concentration, average wind speed and average wind direction were included in the PCA for the coarse mode (Tables 5.1, 5.3) and fine mode (Tables 5.2, 5.4).

Table 5.3: Non-elemental coarse mode parameters and statistics used in APCA.

Variable	Mean	Standard Deviation
Mass concentration ($\mu g/m^3$)	139.6	92.8
550 nm scattering efficiency (m^2/g)	1.6	0.68
360 nm absorption efficiency (m^2/g)	0.26	0.069
550 nm absorption efficiency (m^2/g)	0.19	0.059
660 nm absorption efficiency (m^2/g)	0.17	0.058
Wind speed (m/s)	4.9	2.0
Wind direction (degrees)	224.9	94.2

Table 5.4: Non-elemental fine mode parameters and their statistics used in APCA.

Variable	Mean	Standard Deviation
Mass Concentration ($\mu g/m^3$)	24.7	8.7
550 nm scattering efficiency (m^2/g)	9.9	9.1
360 nm absorption efficiency(m^2/g)	1.7	0.56
550 nm absorption efficiency (m^2/g)	0.98	0.34
660 nm absorption efficiency (m^2/g)	0.79	0.30
Wind speed (m/s)	4.9	2.0
Wind direction (degrees)	224.9	94.2

First, a model of the variability of the elements is constructed so that the set of interrelated measured variables is transformed into a set of independent variables, the principal components [*Echalar et al.*, 1998]. Each variable, measured or resulting from the PCA, is responsible for part of the variance in the data set. The principal components that explain less than one unit of variance are supposed to represent only noise and are excluded before VARIMAX rotation [*Kaiser*, 1960]. The PCA gives two matrices: the "component loadings," which are the correlation coefficients between the original measured variable and the new principal components, and the "component scores," which are a measure of the relative importance of a component in each sample. The stability of PCA depends strongly on the number of samples included in the analysis [*Ito et al.*, 1986]. *Henry* [1991] recommends from experimental methods that there should be enough samples to have at least 30 degrees of freedom. Since the amount of time available to run samples on the PIXE instrument was limited, this analysis falls just within those bounds. The PCA results are quantified using the absolute principal component analysis (APCA) approach developed by *Thurston and Spengler* [1985]. In APCA, quantitative estimates of the contribution from each component to the atmospheric concentration of the aerosol are obtained through regressions of the measured concentrations on previously calculated "absolute principal component scores". Thus, APCA provides a quantitative aerosol source apportionment, attributing a fraction of the measured elemental concentration to each identified source.

Both the coarse mode and fine mode were determined to have four components each. The four sources of the fine mode explain 68% of the variability in

that dataset, while the other 32% is left undetermined (Figure 5.1). The four sources for the coarse mode explain 88% of the variability in the dataset, and the other 12% is left undetermined (Figure 5.1). Based on the complexity of the Xianghe aerosol as determined through analysis of the aerosol physical and optical properties, these values are reasonable.

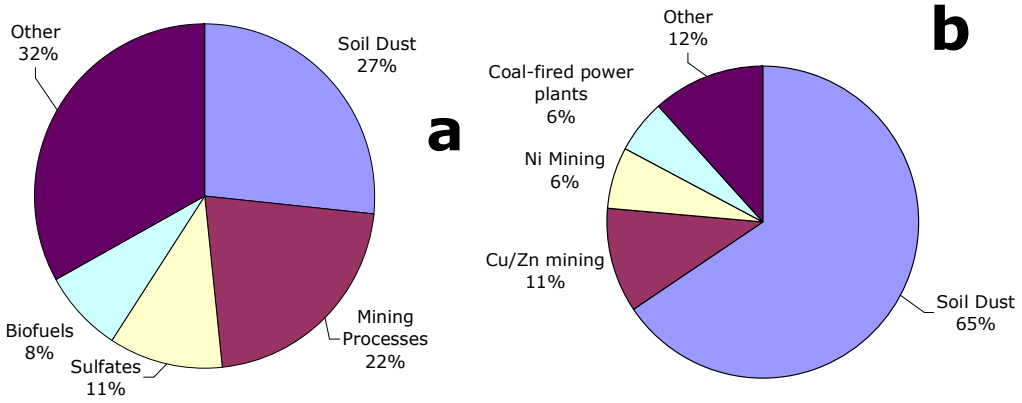

Figure 5.1: Variability of the 27 filter data set that can be explained by PCA for the a) fine mode and b) coarse mode.

A closer examination of the composition within each principal component gives a good picture of the source. The first component of the fine mode, contributing 27% towards the variability in the data set, is comprised of 39% silicon, 15% aluminum, 17% calcium, and 12% iron. The ratio in which these elements are found in this component strongly suggests that the source is soil dust. This further supports the suggestion in previous sections that the spring-time fine mode aerosol has a strong dust component, which was also seen in the aerosol absorption efficiency (Section 2.4) and the fine mode mass concentration (Section 2.2).

The second component of the fine mode aerosol, contributing 22% towards the variability in the data set, is comprised primarily of sulfate, but also has a strong presence of zinc (13%), lead (7%), and even trace amounts of arsenic, copper and

magnesium. The presence of these metals, in the ratios measured, was found by *Nelson* to derive from either zinc or copper mining [1977]. The third component of the fine mode, contributing 11% towards the variability in the data set, is comprised of 67% sulfate. This source of sulfur emission could be coal burning for domestic use, biomass burning, or vehicular exhaust. Lastly, the fourth component, accounting for 8% of the variability in the data set, is comprised of 48% potassium and 27% calcium. The 2:1 ratio of potassium to calcium is indicative of biofuel combustion.

The first component of the coarse mode is the primary component for this data set, accounting for 65% of the variability. This component was comprised of 31% silicon, 15% aluminum, 17% calcium, and 12% iron. With similar ratios to the first component in the fine mode, this component is most likely soil dust. This finding is not surprising, given the results from the absorption efficiency measurements (Section 2.4), but further supports those findings in that soil dust is the largest component of the coarse mode. The composition of the soil dust component in the coarse mode is almost exactly the same as that of the fine mode; the only variation is the percentage of silicon: 31% in the coarse mode, 39% in the fine mode.

The next 3 components explain far less of the variability, but are important to note, nonetheless. The second component, accounting for 11% of the variability, is comprised of 22% copper, 23% zinc, along with significant amounts of arsenic (15%) and lead (12%). The ratio of these metals in the atmosphere was determined by *Nelson* to derive from copper or zinc mining [1977]. The third component, accounting for 6% of the data set variability, probably derives from nickel mining. The component is composed of 47% nickel, along with trace amounts (less than 10%)

of gallium and germanium, which *Andersen et al.* determined was the signature for emissions from nickel mining [1998]. Lastly the fourth component, explaining just 5.6% of the variability, is most likely coarse mode particles originating from coal-fired power plants. The major species in this component is strontium, comprising 42% of the elemental concentration in this component [*Hurst and Davis*, 2006]. Other elements in this fourth component that suggested emissions from coal-fired power plants were sulfate (16%) and potassium (18%).

Chapter 6: Summary and Future Work

6.1 Summary

This study set out to improve our understanding of aerosol optical, physical and chemical properties through in situ measurements. Aerosols were collected using a simple sampling apparatus in two size ranges, the coarse mode (10 μm > d > 2.5 μm) and fine mode (d < 2.5 μm), in a variety of locations. I focused on samples from Xianghe, China, whose proximity to a major urban center (Beijing) in a developing country would provide an interesting study. Separating the measured aerosol into fine and coarse modes has many advantages, one of which is the ability to measure aerosol absorption separately in these two modes. Most models only account for absorbing aerosols in the PM2.5 range, but results presented in this study indicate that the coarse mode is also a significant source of absorbing aerosols. The atmospheric burden of coarse mode particles measured at Xianghe is very high and it needs to be considered in modeling studies.

The variation of mass concentrations between seasons demonstrates the variability and complexity of the Xianghe aerosol. Examining the statistics for each season, we found the highest average coarse mode mass concentration was measured in the fall, at 210 $\mu g/m^3$. The winter and spring had less average coarse mode mass concentrations than the fall at 119 $\mu g/m^3$and 150 $\mu g/m^3$, respectively. These are all still above the average measured in the summer (rainy) season, 96 $\mu g/m^3$. This further supports the conclusions gleaned in Section 2.2, where the absorption efficiency of the cooler months (fall, winter, spring) was higher than the summer months. The greater presence of large particles in those months could be due to an

increase in dust emissions in those cooler periods, or a decrease of coarse particles in the summer, probably due to the summer monsoon rains efficiently removing these large particles from the atmosphere. The fine mode mass concentration saw a similar difference in the average mass concentration, but in this case, the spring season had the lowest measured average at 32 $\mu g/m^3$, compared to the 43 $\mu g/m^3$, 59 $\mu g/m^3$, and 55 $\mu g/m^3$of winter, summer and fall, respectively. The largest average fine mode mass concentration, in winter, can be attributed to the additional emissions of black carbon from residential heating and a lower planetary boundary layer height.

Examining Xianghe in a global context allows us to place the aerosol model into a larger frame of reference. Through ground-based in situ measurements, we determined that Xianghe had the highest total and daytime coarse mode mass concentration compared to Mexico City and Kanpur, India. Kanpur exhibited greater total and daytime coarse mode mass concentration than Mexico City, but both of these locations measured one-half to two-thirds less coarse mode than Xianghe. The strong influence of dust was also seen in the aerosol absorption efficiency measurements, reinforcing our conclusions of a very strong dust presence at Xianghe that is not measured on the ground at these other locations. This was surprising, as these locations were selected for comparison to Xianghe due to the similarity of an upwind dust source. The large difference in the ground-based coarse mode mass concentration could be due to the upwind dust emissions at Kanpur and Mexico City getting lifted above the boundary layer, while the dust at Xianghe stays in the boundary layer and is therefore measurable at the surface.

The highest total and daytime fine mode average mass concentration was measured at Mexico City, followed by Kanpur, India and lastly by Xianghe. While the fine mode mass concentration at Xianghe violated the US NAAQS limits only once during the IOC, the daily total and daytime fine mode mass concentrations at Mexico City and Kanpur surpass this standard frequently during their respective measurement periods. The large amount of fine aerosols at the ground-level at Mexico City and Kanpur can impact respiratory illnesses, agricultural lands, and have significant local climate effects.

The discrepancy seen between the ground-based measurements of mass concentration and AERONET size distribution at numerous locations confirms the need to get a better understanding of the vertical variation of aerosol optical and physical properties. Vertical profiles of aerosols are useful to ascertain where the aerosol is located, and can thereby determine the climate effects of non-ground-based aerosol concentrations. When aerosols get lifted to higher altitudes and transported in layers, their residence time increases, and their influence transitions from local impacts to regional impacts. Saharan Dust plumes can be seen from Caribbean islands, Asian pollution outflow can be seen over Alaska and California. Understanding the processes by which aerosols get lofted and determining how long they remain at a particular level will improve our ability to forecast and model the climate effects of aerosols. The location of aerosols in the vertical structure of the atmosphere determines the radiative impact that they will have. Aerosols located above clouds, below clouds, in the middle of the boundary layer, or right at the surface all have different implications for the global radiation budget.

In this study the vertical profile of aerosols was addressed by two techniques: lidar and the balloon-borne in situ SAS instrument. The SAS instrument was designed for the measurement of the scattering and absorption coefficients. The SAS results in this study focused on the vertical distribution of the scattering coefficient, showing large variability in the profile from day to day, with a prominent presence of strong aerosol layers in the boundary layer. This distribution must be taken into account for an accurate characterization of the aerosol effect on the atmosphere. The instrument was redesigned based on lessons learned from the 2008 campaign, and is undergoing very strict testing at the UMBC-LACO, with the intention of launching again in 2009.

Aerosols play an important role in influencing climate processes, such as cloud development and formation, the hydrologic cycle, the global radiation budget, and even air quality for humans and the biosphere. Studying these particles on a case-by-case basis allows researchers the opportunity to fully understand and characterize the local climate effects. An accurate assessment is needed of how large of a radiative impact aerosols have. This study strove to make such measurements, and for the locations where aerosols were measured, our knowledge is advanced thanks to this work.

6.2 Future Work

The Nuclepore substrate lends itself well to even further analysis than was demonstrated in the work here. Different types of chemical analysis can be performed, and there is the potential for measuring aerosol scattering efficiency in a manner similar to measuring aerosol absorption efficiency. Development of this

technique would allow for single scattering albedo calculations from 350 nm-2500 nm.

The vertical profiles discussed in Section 3.4 could be used in radiative transfer models, such as SBDART, to determine how the aerosol's vertical placement can affect the temperature profile. If there were co-located data, the modeled temperature profiles can be validated with either a microwave radiometer, or by satellite, such as the AIRS retrievals. The profiles themselves can be intercompared with a space-borne lidar, such as CALIPSO, as there was no co-located ground-based lidar operating during any of the launches.

Bibliography

Agranovski, I. E. (2000), New technique for monitoring of aerosol mass concentration, *J. Aerosol Sci., 31*, S783-S784.

Andersen, I., S.R. Berge, and F. Resmann (1998), Speciation of airborne dust from a nickel refinery roasting operation, *Analyst, 123*, 687-689.

Andrews, E., et al. (2006), Comparison of methods for deriving aerosol asymmetry parameter, *J. Geophys. Res., 111*, D05S04, doi:10.1029/2004JD005734.

Arnott, W.P., H. Moosmuller, C.F. Rogers, T. Jin, and R. Bruch (1999), Photoacoustic spectrometer for measuring light absorption by aerosol: instrument design, *Atmos. Environ., 33*, 2845-2852.

Babu, S. S., S. K. Satheesh, and K. K. Moorthy (2002), Aerosol radiative forcing due to enhanced black carbon at an urban site in India, *Geophys. Res. Lett., 29*(18), 1880, doi:10.1029/2002GL015826.

Bergin, M.H., S.E. Schwartz, R.N. Halthore, J.A. Ogren, D.L. Hlavka (2000), Comparison of aerosol optical depth inferred from surface measurements with that determined by Sun photometry for cloud-free conditions at a continental U.S. site, *J. Geophys. Res., 105(D5)*, 6807-6816.

Bergin, M.H. et al. (2001), Aerosol radiative, physical, and chemical properties in Beijing during June 1999, *J. Geophys. Res., 106(D16)*, 17969-17980.

Bergstrom, R.W, P.B. Russell, and P. Hignett (2002), Wavelength dependence of the absorption of black carbon particles: predictions and results from the TARFOX experiment and implications for the aerosol single scattering albedo, *J. Atmos. Sci., 59*, 567-577.

Bond, T.C., T.L. Anderson, and D. Campbell (1999), Calibration and intercomparison of filter-based measurements of visible light absorption by aerosols, *Aerosol Sci. Technol., 30*, 582-600.

Chang, H. and T.T. Charalampopoulos (1990), Determination of the wavelength dependence of refractive indices of flame soot, *Proceedings of The Royal Society of London: Mathematical and Physical Sciences, 430*, 577-591.

Chaudhry, Z., J.V. Martins, Z. Li, S.-C. Tsay, H. Chen, P. Wang, T. Wen, C. Li and R.R. Dickerson (2007), In situ measurements of aerosol mass concentration and radiative properties in Xianghe, southeast of Beijing, *J. Geophys. Res., 112*, D23S90, doi:10.1029/2007JD009055.

Chu, D.A., Y.J. Kaufman, C. Ichoku, L.A. Remer, D. Tanre, and B.N. Holben (2002), Validation of MODIS aerosol optical depth retrieval over land, *Geophys. Res. Lett*., *29*, MOD2-1-4.

Clarke, A.D. (1982), Effects of filter internal reflection coefficient of light absorption measurements made using the integrating plate method, *Appl. Opt., 21,* 3021-3031.

Coakley, J.A and P. Chylek (1975), The two-stream approximation in radiative transfer: Including the angle of incident radiation, *J. Atmos. Sci., 32(2*).

Di Girolamo, L. et al. (2004), Analysis of Mulit-angle Imaging SpectroRadiometer (MISR) aerosol optical depths over greater India during winter 2001-2004, *Geophys. Res. Lett., 31,* L23115, doi:10.1029/2004GL021273.

Dickerson, R.R. et al. (2007), Aircraft observations of dust and pollutants over northeast China: Insights into the meteorological mechanisms of transport, J. Geophys. Res., 112, D24S90, doi:10.1029/2007JD008999.

Doran, J. C. et al (1998), The IMADA-AVER boundary layer experiment in the Mexico City area, *B. Am. Meteorol. Soc.*, 79, 2497-2508.

Dubovik, O., B. Holben, T.F. Eck, A. Smirnov, Y.J. Kaufman, M.D. King, D. Tanre and I. Slutsker (2002), Variability of absorption and optical properties of key aerosol types observed in worldwide locations, *J. Atmos. Sci., 59,* 590-608.

Echalar, F., P. Artaxo, J.V. Martins, M. Yamasoe, F. Gerab, W. Maenhaut, B. Holben (1998), Long-term monitoring of atmospheric aerosols in the Amazon Basin: Source identification and apportionment, *J. Geophys. Res.*, 103 (D24), 31,849-31,864.

Fast, J. D. and S. Zhong (1998), Meteorological factors associated with inhomogenous ozone concentration within the Mexico City basin, *J. Geophys. Res.*, 103, 18,927-18,946.

Fast, J. D. et al. (2007), A meteorological overview of the MILAGRO field campaigns, *Atmos. Chem. Phys.*, 7, 2233-2257.

Forster, P. et al. (2007), Changes in Atmospheric Constituents and in Radiative Forcing. *In: Climate Change 2007: The Physical Science Basis. Contributions of Working Group I to the Fourth Assessment Report of the Intergovernmental Panel on Climate Change* [Solomon, S., D. Qin, M. Manning, Z. Chen, M. Marquis, K.B. Averyt, M. Tignor, and H.L. Miller (eds.)]. Cambridge University Press, Cambridge, United Kingdom and New York, NY, USA.

Ganguly, D., A. Jayaraman, and H. Gadhavi (2005), In situ ship cruise measurements of mass concentration and size distribution of aerosols over Bay of Bengal and their radiative impacts, *J. Geophys. Res.*, D06205, doi:10.1029/2004JD005325.

Hansen, A.D.A, H. Rosen, and T. Novakov (1982), Real-time measurement of the absorption coefficient of aerosol particles, *Appl. Opt., 21,* 3060-3062.

Harman, H. H., Modern Factor Analysis. 3rd ed. Revised. Chicago, University of Chicago, 1976.

Henry, R. C., Multivariate Receptor Models. In: Hopke, P. K. ed., Receptor Modeling for Air Quality Management. Amsterdam, Elsevier, 1991. 117-147.

Holben, B.N. et al. (1998), AERONET- A federated instrument network and data archive for aerosol characterization, *Remote Sens. Environ., 661(1),* 1-16.

Hopke, P.K., Y. Xie, T. Raunemaa, S. Biegalski, S. Landsberger, W. Maenhaut, P. Artaxo, D. Cohen (1997), Characterization of the Gent Stacked Filter Unit PM10 sampler, *Aerosol Sci. Technol., 27,* 726-735.

Huebert, B.J., T. Bates, P.B. Russell, G. Shi, Y.J. Kim, K. Kawamura, G. Carmichael, and T. Nakajima (2003), An overview of ACE-Asia: Strategies for quantifying the relationships between Asian aerosols and their climatic impacts, *J. Geophys. Res., 108(D23),* ACE1-1.

Hurst, R.W. and T.E. Davis (2006), Strontium isotopes as tracers of airborne fly ash from coal-fired power plants, *Environmental Geology, 3(6),* 363-367.

Ichoku, C., D.A. Chu, S. Mattoo, Y.J. Kaufman, L.A. Remer, D. Tanre, I. Slutsker, and B.N. Holben (2002), A spatio-temporal approach for global validation and analysis of MODIS aerosol products, *Geophys. Res. Lett., 29,* MOD1-1-4.

Ito, K., T. J. Kneip, P. J. Lioy (1986), The effects of number of samples and random errors on the Factor Analysis/Multiple Regression (Fa/MR) Receptor Modeling Technique, *Atmos. Environ.*, 20, 1433-1440.

Jacobson, M.Z. (1999), Isolating nitrated and aromatic aerosols and nitrated aromatic gases as sources of ultraviolet light absorption, *J. Geophys. Res., 104(D3),* 3527-3542.

Jacobson, M.Z. (2000), A physically-based treatment of elemental carbon optics: Implications for global direct forcing of aerosols, *Geophys. Res. Lett., 27,* 217-220.

Johansson, S.A.E, J.L. Campbell, K.G. Malmqvist (1995), *Particle-Induced X-ray Emission Spectrometry (PIXE),* 451 pages, Wiley-Interscience.

John, W., S. Hering, G. Reischl, G. Sasaki, and S. Goren (1983), Characteristics of Nuclepore filters with large pore size, II. Filteration Properties, *Atmos. Environ., 17*, 373-382.

Kaiser, H.F. (1960), The application of electronic computers to factor analysis, *Educ. Psychol. Meas.*, 20, 141-151.

Kaufman, Y.J., D. Tanre, L.A. Remer, E.F. Vermote, D.A. Chu, and B.N. Holben (1997), Operational remote sensing of tropospheric aerosol over land from EOS moderate resolution imaging spectroradiometer, *J. Geophys. Res., 102*, 17051-17067.

Kindel, B.C., Z. Qu, and A.F.H. Goetz (2001), Direct solar spectral irradiance and transmittance measurements from 350 to 2500 nm, *Appl. Opt., 40(21)*, 3483-3494.

Kirchstetter, T.W., T. Novakov, and P.V. Hobbs (2004), Evidence that the spectral dependence of light absorption by aerosols is affected by organic carbon, *J. Geophys. Res., 109*, D21208.

Koren, I., J.V. Martins, L.A. Remer, H. Afargan (2008), Smoke invigoration versus inhibition of clouds over the Amazon, *Science, 321 (5891)*, 946-949, doi:10.1126/science.1159185.

Levy, R.C., L.A. Remer, S. Mattoo, E.F. Vermote and Y.J. Kaufman (2007), Second-generation operational algorithm: Retrieval of aerosol properties over land from inversion of Moderate Resolution Imaging Spectroradiometer spectral reflectance, *J. Geophys Res., 112*, D13211, doi:10.1029/2006JD007811.

Li, C., L.T. Marufu, R.R. Dickerson, Z. Li, T. Wen, Y. Wang, P. Wang, H. Chen, J.W. Stehr (2007), In-situ measurements of trace gases and aerosol optical properties at a rural site in Northern China during EAST-AIRE 2005, *J. Geophys Res.* D22S04, doi: 10.1029/2006JD007592.

Li, Z. et al. (2007), Aerosol optical properties and its radiative effects in Northern China, *J. Geophys. Res.* 112, D22S01, doi: 10.1029/2006JD007382.

Lin, C.I., M. Baker, and R.J. Charlson (1973), Absorption coefficient of atmospheric aerosol: a method for measurement, *Appl. Opt., 12(6)*, 1356-1363.

Ma, C.-J., M. Kasahara, R. Holler, and T. Kamiya (2001), Characteristics of single particles sampled in Japan during the Asian dust-storm period, *Atmos. Environ., 35*, 2707-2714.

Marley, N. A., J. S. Gaffney, P. J. Drayton, M. M. Cunningham, K. A. Orlandini, and R. Paode (2000), Measurement of 210Pb, 210P0, and 210Bi in size fractionated

atmospheric aerosols; An estimate of fine-aerosol residence times, *Aerosol Sci. Tech.*, 32, 569-583.

Martins, J.V., P. Artaxo, C. Liousse, J.S. Reid, P.V. Hobbs, and Y.J. Kaufman (1998), Effects of black carbon content, particle size, and mixing on light absorption by aerosols from biomass burning in Brazil, *J. Geophys. Res*., *103(D24)*, 32041-050.

Martins, J.V., P. Artaxo, Y. Kaufman, and A.D. Castanho (2009), Spectral absorption properties of urban aerosol particles from 350-2500 nm, Manuscript submitted for publication to *Geophys. Res. Lett*., January 30th, 2009.

Molina, L. T., and M. J. Molina, Air quality impacts: Local and global concern, Chapter 1 in: Air quality in the Mexico Megacity, an integrated assessment, edited by: L. T. Molina, M. J. Molina, Kluwer Academic, The Netherlands, 2002.

Molina, L. T., et al (2007), Air quality in North America's most populous city – overview of the MCMA-2003 campaign, *Atmos. Chem. Phys., 7*, 2447-2473.

Nakajima, T. et al. (2003), Significance of direct and indirect radiative forcings of aerosols in the East China Sea region, *J. Geophys. Res.*, *108*(D23), 8658.

Nelson, K.W. (1977), Industrial contributions of Arsenic to the environment, *Environmental Health Perspectives*, 19, 31-34.

Ning, D., L. Zhong, and Y. Chung (1996), Aerosol size distribution and elemental composition in urban areas of northern China, *Atmos. Environ*., *30*, 2355-2362.

Pahlow, M., G. Fiengold, A. Jefferson, E. Andrews, J.A. Ogren, J. Wang, Y.-N. Lee, R.A. Ferrare, and D.D. Turner (2006), Comparison between lidar and nephelometer measurements of aerosol hygroscopicity at the Southern Great Plains Atmospheric Radiation Measurement site, *J. Geophs. Res.*, *111*, D05S15, doi:10.1029/2004JD005646.

Parker, R.D., G.H. Buzzard, T.G. Dzubay, and J.P. Bell (1977), A two stage respirable aerosol sampler using Nuclepore filters in series, *Atmos. Environ.*, *11*, 617-621.

Posfai, M., J. R. Anderson, P.R. Buseck, H. Sievering (1999), Soot and sulfate aerosol particles in the remote marine troposphere, *J. Geophys. Res.*, 104, 21683-21685.

Querol, X. et al (2008), PM speciation and sources in Mexico during the MILAGRO-2006 Campaign, *Atmos. Chem. Phys., 8*, 111-128.

Ramanathan, V., P.J. Crutzen, J.T. Kiehl, D. Rosenfeld (2001a), Aerosols, climate, and the hydrological cycle, *Science, 294*, 2119-2124.

Ramanathan, V., et al (2001b), Indian Ocean Experiment: An integrated analysis of the climate forcing and effects of the great Indo-Asian haze, *J. Geophys. Res., 106, D22,* 28,371-28,398.

Reid, J.S., P.V. Hobbs, C. Liousse, J.V. Martins, R.E. Weiss, and T.F. Eck (1998), Comparison of techniques for measuring shortwave absorption and black carbon content of aerosols from biomass burning in Brazil, *J. Geophys. Res*., SCAR-B Special Issue, *103(D24)*, 32031-040.

Remer, L.A. et al. (2002), Validation of MODIS aerosol retrieval over ocean, *Geophys. Res. Lett., 29*, MOD3-1-4.

Samet, J.M., F. Dominici, F.C. Curriero, I. Coursac, and S.L. Zeger (2000), Fine particulate air pollution and mortality in 20 US cities, 1987-1994, *N. Engl. J. Med., 343(24)*, 1742-1749.

Sappey, A.D., E.S. Hill, T. Settersten, and M.A. Linne (1998), Fixed-frequency cavity ringdown diagnostic for atmospheric particulate matter, *Optics Letters, 23* (*12*), 954-956.

Schnaiter, M., C. Linke, O. Mohler, K.-H. Naumann, H. Saathoff, R. Wagner, U. Schurath, and B. Wehner (2005), Absorption amplification of black carbon internally mixed with secondary organic aerosol, *J. Geophys. Res.*, 110, D19204, doi: 10.1029/2005JD006046.

Schwartz, S. E. and P. R. Buseck (2000), Absorbing phenomena, *Science*, 288, 989-990.

Seinfeld, J.H., and S.N. Pandis, Atmospheric chemistry and physics: From air pollution to climate change, xxvii, 1326 pp., John Wiley, New York, 1998.

Shi, Z., L. Shao, T.P. Jones, A.G. Whittaker, S. Lu, K.A. Berube, T. He, and R.J. Richards (2003), Characterization of airborne individual particles collected in an urban area, a satellite city and a clean air area in Beijing, 2001, *Atmos. Environ., 37*, 4097-4108.

Smirnov, A., B.N. Holben, D. Savoie, J.M. Prospero, Y.J. Kaufman, D. Tanre, T.F. Eck, and I. Slutsker (2000), Relationship between column aerosol optical thickness and in situ ground based dust concentrations over Barbados, *Geophys. Res. Lett., 27*, 1643-1646.

Spindler, C., A. Abo Riziq, and Y. Rudich (2007), Retrieval of aerosol complex refractive index by combining cavity ring down aerosol spectrometer measurements with full size distribution information, *Aerosol Sci. Tech., 41*, 1011-1017, doi:10.1080/02786820701682087.

Thurston, G. D. and J. D. Spengler (1985), A quantitative assessment of source contributions to inhalable particulate matter pollution in metropolitan Boston, *Atmos. Environ*, 19, 9-25.

TRACE-P Science Team (2003), Preface to the NASA Global Tropospheric Experiment Transport and Chemical Evolution Over the Pacific (TRACE-P): Measurements and Analysis, *J. Geophys. Res.*, *108*(D20), 8780, doi:10.1029/2003JD003851.

Virkkula, A., N.C. Ahlquist, D.S. Covert, W.P. Arnott, P.J. Sheridan, P.K. Quinn, and D.J. Coffman (2005), Modification, calibration and a field test of an instrument for measuring light absorption by particles, *Aerosol Sci. Technol.*, *39*, 68-83.

Volckens, J. and T.M. Peters (2005), Counting and particle transmission efficiency of the aerodynamic particle sizer, *J. Aerosol Sci.*, *36*(12), 1400-1408.

Weiss, R., and A. Waggoner (1984), Aerosol optical absorption: accuracy of filter measurement by comparison with in-situ extinction, *Aerosols*, Edited by B. Liu, D. Pui, and H. Fissan, pp 397.

West, R.A, L.R. Doose, A.M. Eibl, M.G. Tomasko, M.I. Mishchenko (1997), Laboratory measurements of mineral dust scattering phase function and linear polarization, *J. Geophys, Res.*, *102(D14)*, 16,871-16,881.

Whiteman, C. D., S. Zhong, X. Bian, J. D. Fast, and J. C. Doran (2000), Boundary layer evolution and regional scale diurnal circulations over the Mexican plateau, *J. Geophys. Res.*, 105, 10081-10102.

Williams, J., M. de Reus, R. Krejci, H. Fischer, and J. Strom (2002), Applications of the variability-size relationship to atmospheric aerosol studies: estimating aerosol lifetimes and ages, *Atmos. Chem. Phys.*, 2, 133-145.

Winker, D.M., J.R. Pelon, and M.P. McCormick (2003), The CALIPSO mission: spaceborne lidar for observation of aerosols and clouds, *Proceedings of SPIE, 4893*, 1-11.

Yamasoe, M.A., P. Artaxo, A.H. Miguel, and A.G. Allen (2000), Chemical composition of aerosol particles from direct emissions of vegetation fires in the Amazon Basin: Water-soluble species and trace elements, *Atmos. Environ.*, *34*, 1641-1653.

Ye, B., X. Ji, H. Yang, X. Yao, C.K. Chan, S.H. Cadle, T. Chan, and P.A. Mulawa (2003), Concentration and chemical composition of PM2.5 in Shanghai for a 1-year period, *Atmos. Environ.*, *37*, 499-510.

Zhao, Z. and Z.Li (2007), Estimation of aerosol single scattering albedo from solar direct spectral radiance and total broadband irradiances, *J. Geophys. Res.*, 112, D22S03, doi: 10.1029/2006JD007384.

Zwally, H.J. et al. (2002), ICESat's laser measurements of polar ice, atmosphere, ocean, and land, *J. Geodynamics*, *34*, 405-445.